



Shock vibration and damage responses of nuclear island subjected to an aircraft crash

Yi Sui, Degao Zou^{1,*}, Kai Chen

Institute of Earthquake Engineering, Dalian University of Technology, Dalian 116024, China

ARTICLE INFO

Keywords:

Aircraft crash
Damage propagation
AP1000
Scaled boundary finite element method (SBFEM)
Combination bonding method
SSI effect

ABSTRACT

Although more attention has been given towards the analysis of large commercial aircraft impacts since the September 11 attacks, little work has been done on the vibration response of internal structures and equipment of nuclear power plants (NPPs) during an impact. With a focus on new NPPs, this paper develops a remeshing algorithm for contact surfaces, which utilizes the advantages of scaled boundary finite element (SBFE) polyhedral elements to fully realize the potential of Octree and structured grid discretization methods. The vibration response of nuclear island internal structures is examined. The influence of the interaction between the foundation and the structure on the overall dynamic response is analyzed. Meanwhile, different ranges of foundation size are investigated for balance between computational efficiency and accuracy. The vibration propagation mechanism is found by studying the influence of different artificial boundary types and damping conditions of foundation. The results show that the interaction has a significant influence on the vibration response, and that a foundation size of 1B (height of the steel containment vessel) on all sides provides the optimal balance between computational and accuracy requirements. Furthermore, the damping ratio of the foundation plays a key role in vibration propagation. Finally, the combined bonding method is highly flexible, and allows cross-scale integration of different mesh sizes.

1. Introduction

By the end of 2019, there were 442 operational nuclear power plants in the world contributing to a net capacity of about 390 GW. Since then, 53 additional plants have been planned for construction to generate a net capacity of about 56 GW. The United States takes the largest share of nuclear power plants at 96 units while China has the largest number under construction at 10 units [1]. However, since the 9/11 attacks in the United States, the ability of nuclear power plants to withstand a malicious impact by a large commercial aircraft has become a focal issue that has attracted attention from nuclear safety regulators in various countries, nuclear power plant research and development (R&D) organizations, and even the general public. In 2009, the US Nuclear Regulatory Commission issued Federal Regulation 10CFR 50.150 [2], and in 2016 the National Nuclear Safety Administration of China issued a new version of HAF 102-2016 [3]. The regulations include an assessment of potential impact of maliciously piloted commercial aircraft. At present, worldwide efforts have led to extensive and in-depth research results

[4–9].

When a nuclear power plant suffers from a malicious impact by a commercial or civilian aircraft, a series of catastrophic accidents will be initiated, such as 1) impact-induced global and local structural failures; 2) effects of violent shock caused by impacts on the structures, systems and components (SSCs); and 3) fire-related problems due to fuel leakage caused by the collision [10,11]. Analysis of impact-induced vibrations requires a fine mesh size of the impact region and the damage diffusion area to accurately emulate the evolution of damage. On the other hand, the modelling and grid discretization of the internal structure involves a large number of cross-scale connection problems. However, traditional grid discretization methods inevitably lead a tedious, manual modelling and very high computational costs. Thus, notable results have been limited in this field. In addition, the performance of key modelled equipment also requires validation from experimental data, which are not found in the literature.

Petrangeli [12] studied the severe vibration of internal nuclear power plant structures when the plant is struck by aircraft. Since the

* Corresponding author.

E-mail addresses: zoudegao@dlut.edu.cn (D. Zou), chenkai@mail.dlut.edu.cn (K. Chen).

¹ His research mainly focuses on the seismic design of high rockfill dams and nuclear power plants, the engineering properties of coarse-grained soil, and geotechnical testing technology. E-mail: zoudegao@dlut.edu.cn.

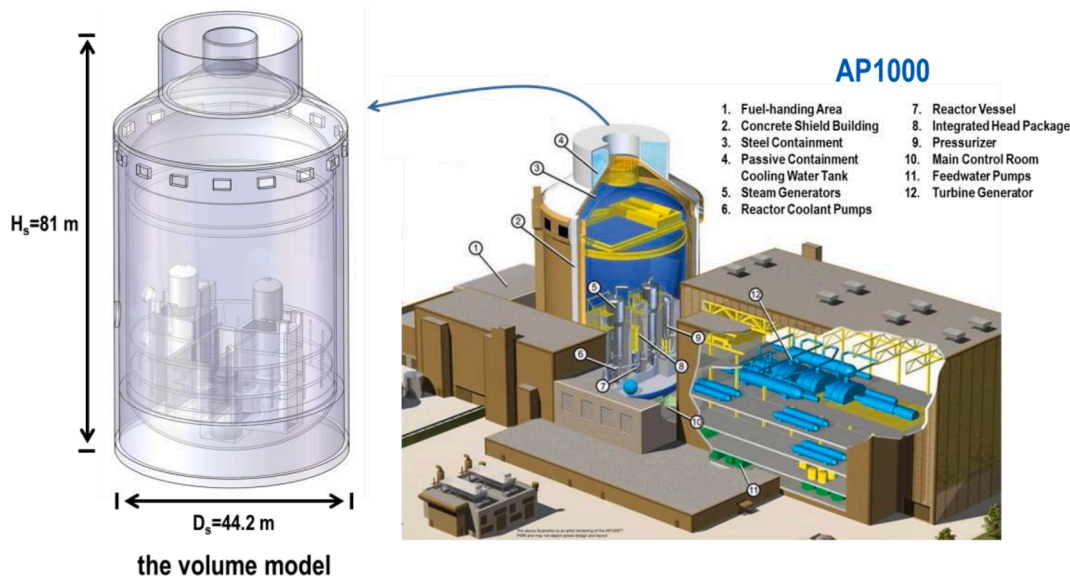


Fig. 1. Profiles of nuclear power plants.

internal structure and the external wall are connected by a common raft foundation, it is assumed that an isolation device should be set inside to reduce the influence caused by vibration. Kostov [13] established a refined three-dimensional finite element model of the generation III reactor VVER A92, and used the model to study structural integrity problems and evaluate the safety of important equipment in the event of aircraft impact. Impact loads can be analyzed via three different methods: force–time history as determined by Riera method, force–time history as computed by finite element analysis [14], and missile-target interaction analysis. Typically, a variety of impact locations and loading intensities are considered in impact load analyses. The safety of the internal structure can be evaluated using the floor acceleration and displacement response spectra and the absolute cumulative velocity (CAV). Shin [15] analyzed damage conditions and vibration

characteristics of auxiliary plants after impact from commercial aircraft by using force–time history analysis (FTHA) and missile-target interaction analysis (MTIA) respectively. Thai [16] conducted a missile-target interaction analysis of aircraft impact on the auxiliary building of KSNP in South Korea, and evaluated the influence of overall and local damage and vibration on structural safety. The simulation results show that the vibration acceleration values exceed the requirements for shutdown according to the Nuclear Regulatory Commission. In the commission, the impact of B767-400 aircraft on structures similar to the auxiliary building would be too devastating to guarantee the safety of internal equipment. However, for questions of whether the internal equipment of the nuclear power plants meets vibration safety requirements, whether the vibration and acceleration is enough to reach the shutdown threshold, and whether the NEI07-13 [17] instruction

In the 3D domain:

The displacement of any point:

$$\{u(\hat{x}, \hat{y}, \hat{z})\} = [u_x(\hat{x}, \hat{y}, \hat{z}), u_y(\hat{x}, \hat{y}, \hat{z}), u_z(\hat{x}, \hat{y}, \hat{z})]^T$$

Linear differential operator

$$[L] = \begin{bmatrix} \frac{\partial}{\partial \hat{x}} & \frac{\partial}{\partial \hat{y}} & \frac{\partial}{\partial \hat{z}} \\ \frac{\partial}{\partial \hat{y}} & \frac{\partial}{\partial \hat{x}} & 0 \\ \frac{\partial}{\partial \hat{z}} & \frac{\partial}{\partial \hat{x}} & \frac{\partial}{\partial \hat{y}} \end{bmatrix}^T$$

Strains

$$\{\varepsilon(\hat{x}, \hat{y}, \hat{z})\} = [L]\{u(\hat{x}, \hat{y}, \hat{z})\}$$

$$\{\varepsilon(\hat{x}, \hat{y}, \hat{z})\} = [\varepsilon_x(\hat{x}, \hat{y}, \hat{z}), \varepsilon_y(\hat{x}, \hat{y}, \hat{z}), \varepsilon_z(\hat{x}, \hat{y}, \hat{z}), \gamma_{yz}(\hat{x}, \hat{y}, \hat{z}), \gamma_{xz}(\hat{x}, \hat{y}, \hat{z}), \gamma_{xy}(\hat{x}, \hat{y}, \hat{z})]^T$$

The symmetric, positive-definite elasticity matrix $[D]$ is introduced to obtain stress vector, as shown:

$$\{\sigma(\hat{x}, \hat{y}, \hat{z})\} = [D]\{\varepsilon(\hat{x}, \hat{y}, \hat{z})\}$$

Fig. 2. The elastic-static governing equations.

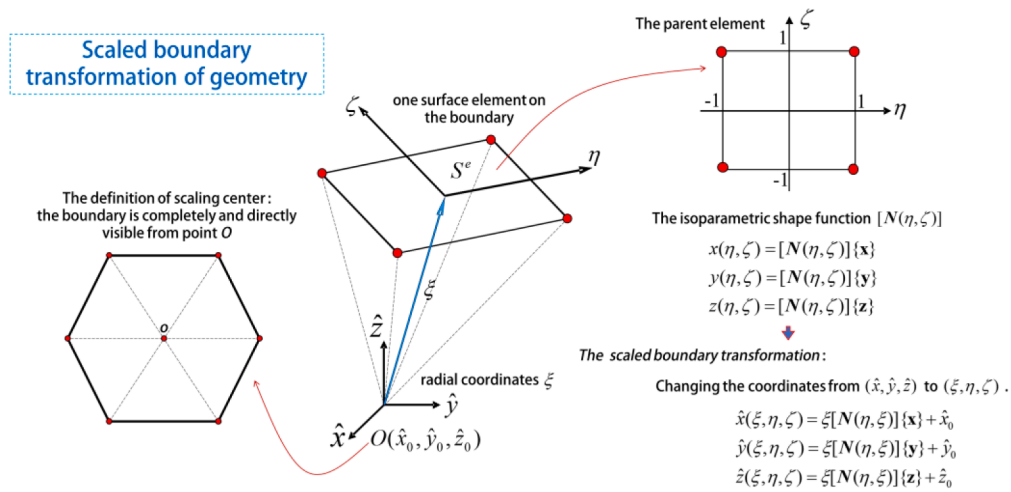


Fig. 3. Description of the coordinate system of SBFEM.

Scaled boundary transformation of geometry

The Jacobian matrix:

$$[J(\eta, \zeta)] = \begin{bmatrix} x(\eta, \zeta) & y(\eta, \zeta) & z(\eta, \zeta) \\ x(\eta, \zeta)_{,\eta} & y(\eta, \zeta)_{,\eta} & z(\eta, \zeta)_{,\eta} \\ x(\eta, \zeta)_{,\zeta} & y(\eta, \zeta)_{,\zeta} & z(\eta, \zeta)_{,\zeta} \end{bmatrix}$$

The linear differential operator:

$$[L] = b_1(\eta, \zeta) \frac{\partial}{\partial \xi} + \frac{1}{\xi} \left(b_2(\eta, \zeta) \frac{\partial}{\partial \eta} + b_3(\eta, \zeta) \frac{\partial}{\partial \zeta} \right)$$

$b_1(\eta, \zeta) = \frac{1}{|J|}$

$$b_1(\eta, \zeta) = \frac{1}{|J|} \begin{bmatrix} y_{,\eta} z_{,\zeta} - z_{,\eta} y_{,\zeta} & 0 & 0 \\ 0 & z_{,\eta} x_{,\zeta} - x_{,\eta} z_{,\zeta} & 0 \\ 0 & 0 & x_{,\eta} y_{,\zeta} - y_{,\eta} x_{,\zeta} \\ 0 & x_{,\eta} y_{,\zeta} - y_{,\eta} x_{,\zeta} & z_{,\eta} x_{,\zeta} - x_{,\eta} z_{,\zeta} \\ x_{,\eta} y_{,\zeta} - y_{,\eta} x_{,\zeta} & 0 & y_{,\eta} z_{,\zeta} - z_{,\eta} y_{,\zeta} \\ z_{,\eta} x_{,\zeta} - x_{,\eta} z_{,\zeta} & y_{,\eta} z_{,\zeta} - z_{,\eta} y_{,\zeta} & 0 \end{bmatrix}$$

$b_2(\eta, \zeta) = \frac{1}{|J|}$

$$b_2(\eta, \zeta) = \frac{1}{|J|} \begin{bmatrix} zy_{,\zeta} - yz_{,\zeta} & 0 & 0 \\ 0 & xz_{,\zeta} - zx_{,\zeta} & 0 \\ 0 & 0 & yx_{,\zeta} - xy_{,\zeta} \\ 0 & yx_{,\zeta} - xy_{,\zeta} & xz_{,\zeta} - zx_{,\zeta} \\ yx_{,\zeta} - xy_{,\zeta} & 0 & zy_{,\zeta} - yz_{,\zeta} \\ xz_{,\zeta} - zx_{,\zeta} & zy_{,\zeta} - yz_{,\zeta} & 0 \end{bmatrix}$$

$b_3(\eta, \zeta) = \frac{1}{|J|}$

$$b_3(\eta, \zeta) = \frac{1}{|J|} \begin{bmatrix} yz_{,\eta} - zy_{,\eta} & 0 & 0 \\ 0 & zx_{,\eta} - xz_{,\eta} & 0 \\ 0 & 0 & xy_{,\eta} - yx_{,\eta} \\ 0 & xy_{,\eta} - yx_{,\eta} & zx_{,\eta} - xz_{,\eta} \\ xy_{,\eta} - yx_{,\eta} & 0 & yz_{,\eta} - zy_{,\eta} \\ zx_{,\eta} - xz_{,\eta} & yz_{,\eta} - zy_{,\eta} & 0 \end{bmatrix}$$

Fig. 4. Description of the linear differential operator of SBFEM.

Nodal displacement function in the radial direction

The displacements at a point (ξ, η, ζ) inside a pyramid

can be interpolated from the displacement function $u(\xi)$

$$u(\xi, \eta, \zeta) = N^u(\eta, \zeta) u(\xi)$$

$$N^u(\eta, \zeta) = [N_1[I], N_2[I], N_3[I], N_4[I]]$$

$$\begin{aligned} N_1 &= \frac{1}{4}(1-\xi)(1-\zeta) & N_2 &= \frac{1}{4}(1+\xi)(1-\zeta) \\ N_3 &= \frac{1}{4}(1+\xi)(1+\zeta) & N_4 &= \frac{1}{4}(1-\xi)(1+\zeta) \end{aligned}$$

The strains of an element can be expressed as:

$$\varepsilon(\xi, \eta, \zeta) = B_1(\eta, \zeta) u(\xi) + \frac{1}{\xi} B_2(\eta, \zeta) u(\xi)$$

$$B_1(\eta, \zeta) = b_1(\eta, \zeta) N^u(\eta, \zeta) \quad B_2(\eta, \zeta) = b_2(\eta, \zeta) N^u(\eta, \zeta)_{,\eta} + b_3(\eta, \zeta) N^u(\eta, \zeta)_{,\zeta}$$

Fig. 5. Nodal displacement function in the radial direction.

Scaled boundary polyhedron shape functions

The variational principle is introduced, and the equilibrium equation can be expressed as:

$$E_0 \xi^2 u(\xi)_{,\xi\xi} + (2E_0 + E_1^T - E_1) \xi u(\xi)_{,\xi} + (E_1^T - E_2) u(\xi) + \omega^2 M_0 \xi^2 u(\xi) = 0$$

$$\begin{aligned} E_0 &= \int_{-1}^{+1} \int_{-1}^{+1} B_1^T D B_1 |J| d\eta d\zeta & E_1 &= \int_{-1}^{+1} \int_{-1}^{+1} B_2^T D B_1 |J| d\eta d\zeta \\ E_2 &= \int_{-1}^{+1} \int_{-1}^{+1} B_2^T D B_2 |J| d\eta d\zeta & M_0 &= \int_{-1}^{+1} \int_{-1}^{+1} \rho N^T N |J| d\eta d\zeta \end{aligned}$$

where B_1 and B_2 are the strain displacement transition matrices, D is the constitutive matrix and N is the shape function of a surface element.

Fig. 6. Scaled boundary polyhedron shape functions.

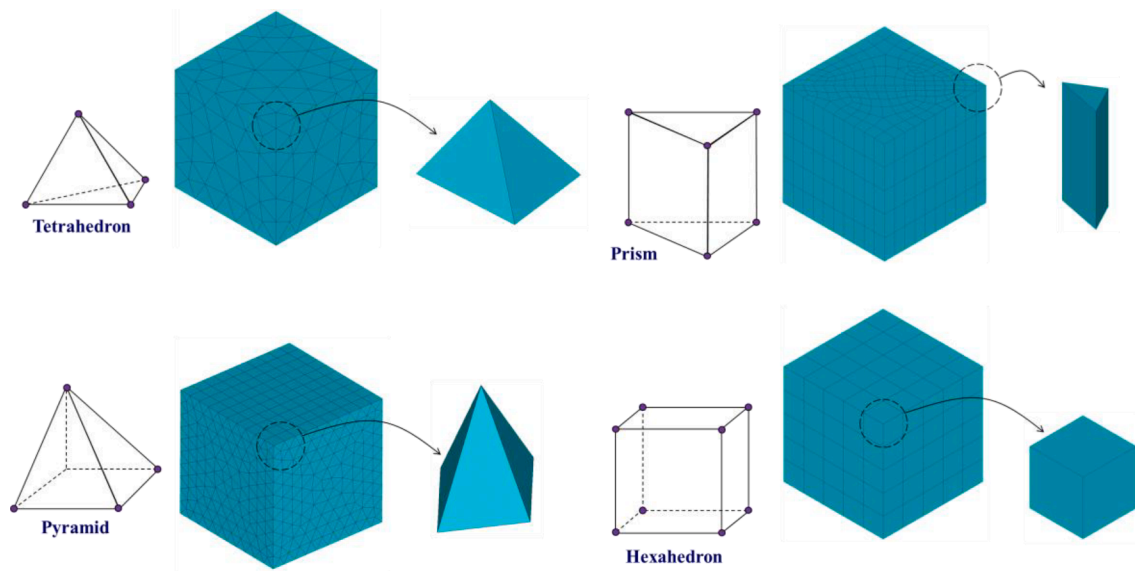


Fig. 7. Traditional element types and model.

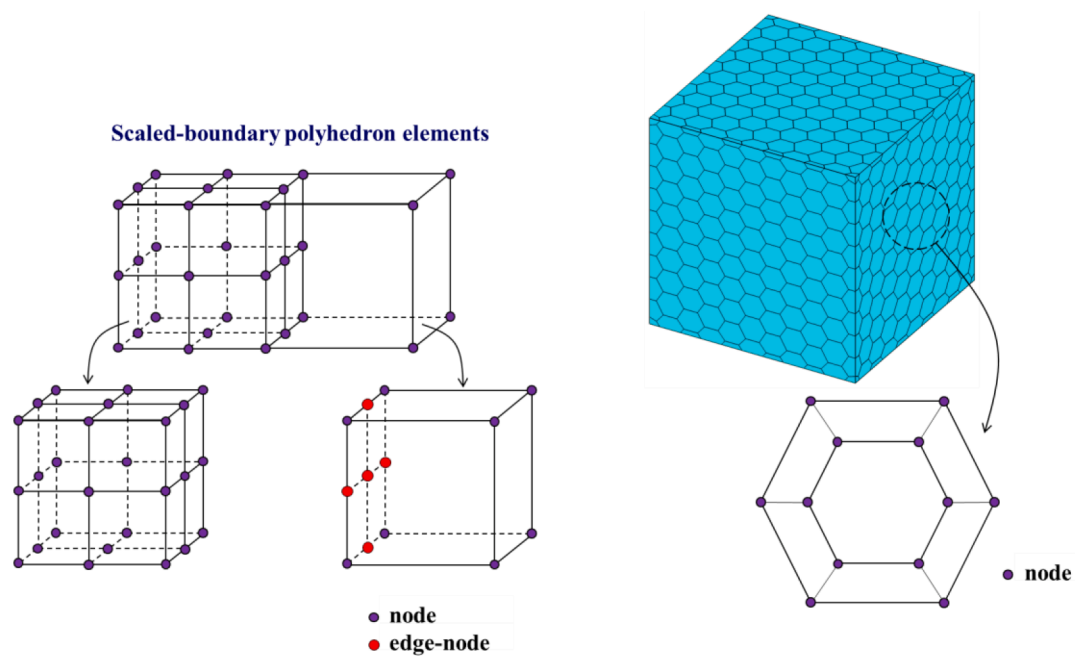


Fig. 8. Scaled-boundary finite elements and model.

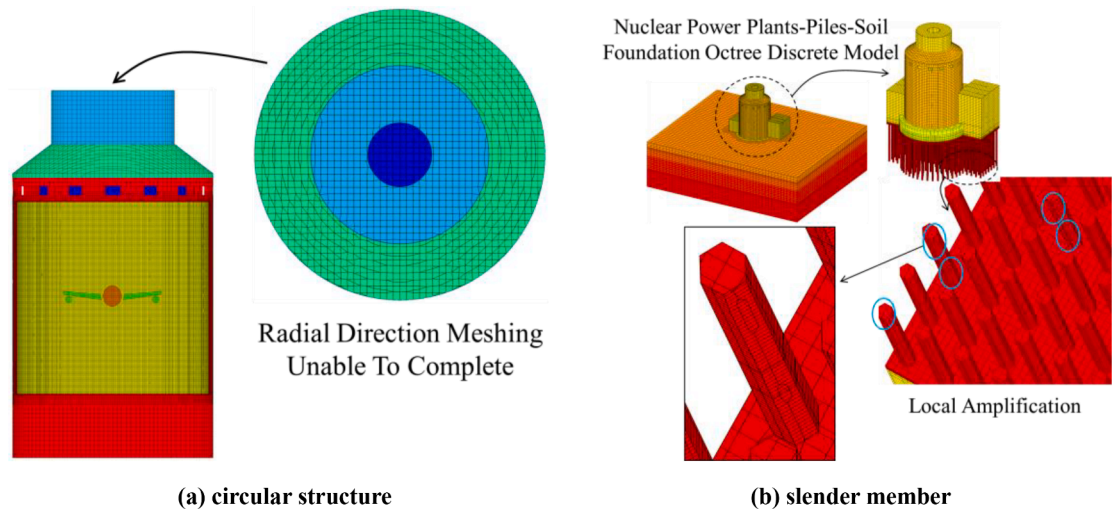


Fig. 9. Octree mesh discrete model.

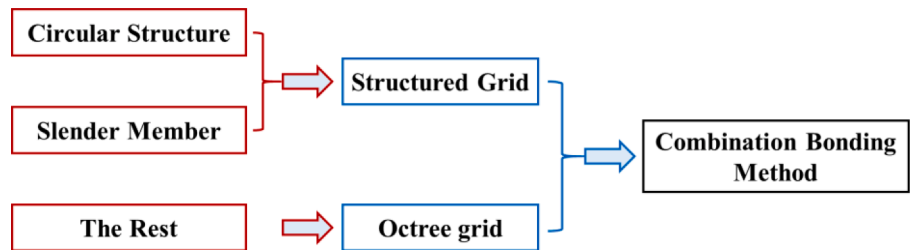


Fig. 10. Breakdown of proposed combination bonding method.

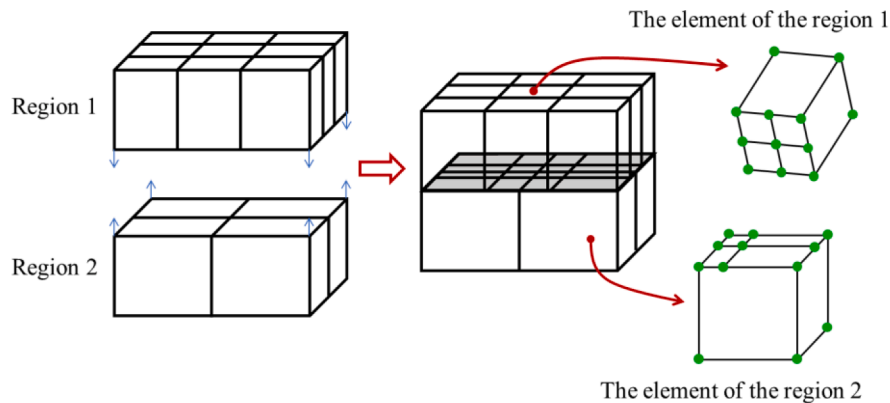


Fig. 11. Diagram of process combining regions 1 and 2, which are meshed differently.

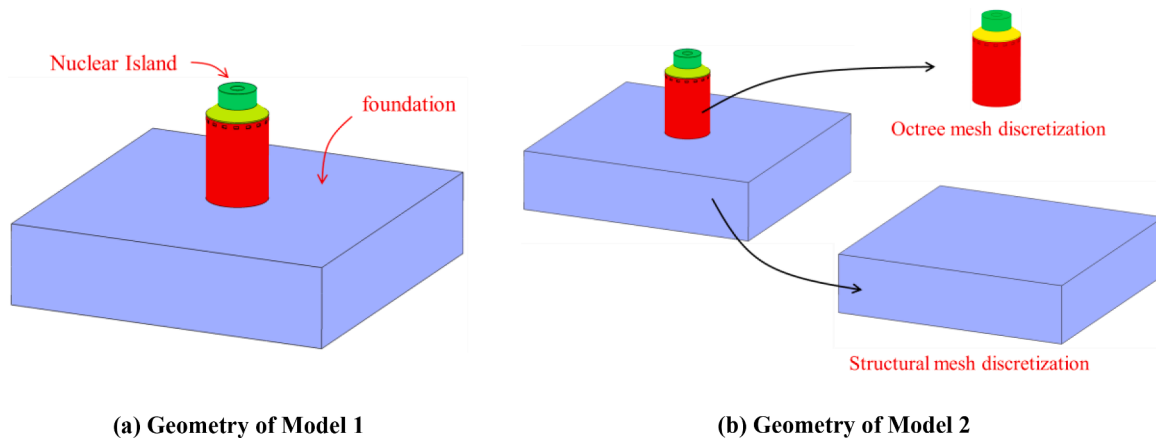


Fig. 12. Horizontal verification group.

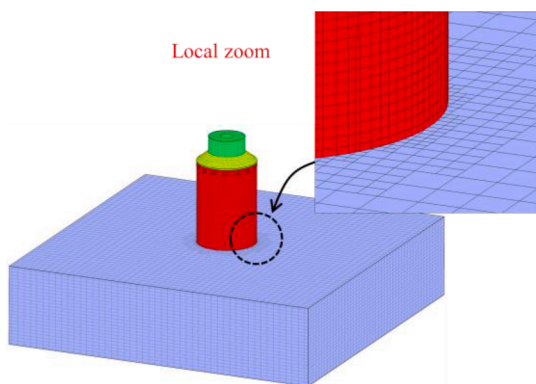


Fig. 13. Model 1: Octree mesh discretization.

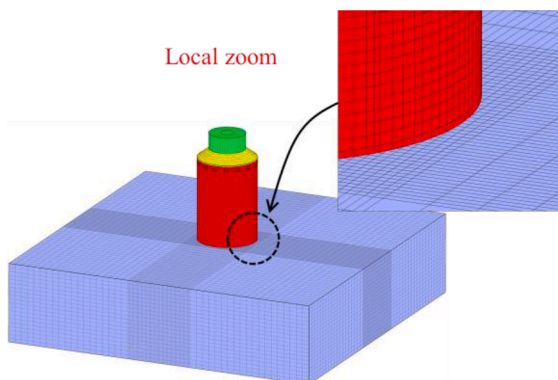


Fig. 14. Model 2: Combination bonding method.

manual can still be used as a reference in the case of such an impact, there are not yet any reliable guidance from research results nor are there any established the evaluation methods.

Our previous research [18] demonstrated that refined models and fine-scale elements more accurately reflect failure processes and behaviours [19]. Furthermore, the prior efforts are the first known successful attempts to combine the scaled boundary polyhedron finite element analysis method (SBFEM) with the octree technique to perform refined analysis of damage evolution in nuclear engineering structures. Key insights into damage evolution laws are obtained. Building upon the prior work, this paper aims to bridge the gap in the availability of vibration response analysis and evaluation methods for internal equipment of nuclear power plants impacted by large commercial aircraft. This paper combines bonding cross-scale modeling methods to establish a computational model of the AP1000 Nuclear Island, including the steam generation module (CA01) and other internal structures. The vibration responses of the internal structure are examined. The important influence of structure-soil interaction effect (SSI effect) on the vibration response of internal structures during impact is further analyzed. Then, the paper discusses feasible ranges at which the rock foundation can be truncated during modelling. Mechanisms by which vibrations are transmitted and the effects of such mechanisms on the vibration response are analyzed. Finally, a set of evaluation criteria are established for safety assessment.

2. Containment vessel model

2.1. Profiles of nuclear power plants

The nuclear island (NI) of the AP1000 is composed primarily of a reactor building and an auxiliary building. The reactor building has an exterior reinforced concrete (RC) containment vessel, an interior steel containment vessel and internal structural components as shown in Fig. 1. The reinforced concrete (RC) containment vessel is also called a shield building and has an outer diameter of 44.2 m and wall thickness of 0.914 m. The conical roof wall thickness is also 0.914 m. In the internal components, the top and bottom of the steel containment vessel are oval-shaped. The thicknesses of the top and bottom oval-shaped structure are 41.3 mm and 47.6 mm, respectively. The interior steel containment vessel has a clearance of 1.37 m from the shield building. The reactor building is affixed to the RC basement slab, which is 1.8 m thick.

2.2. Summary of the SBFEM

The essential theory of the SBFEM is summarized in this section. The

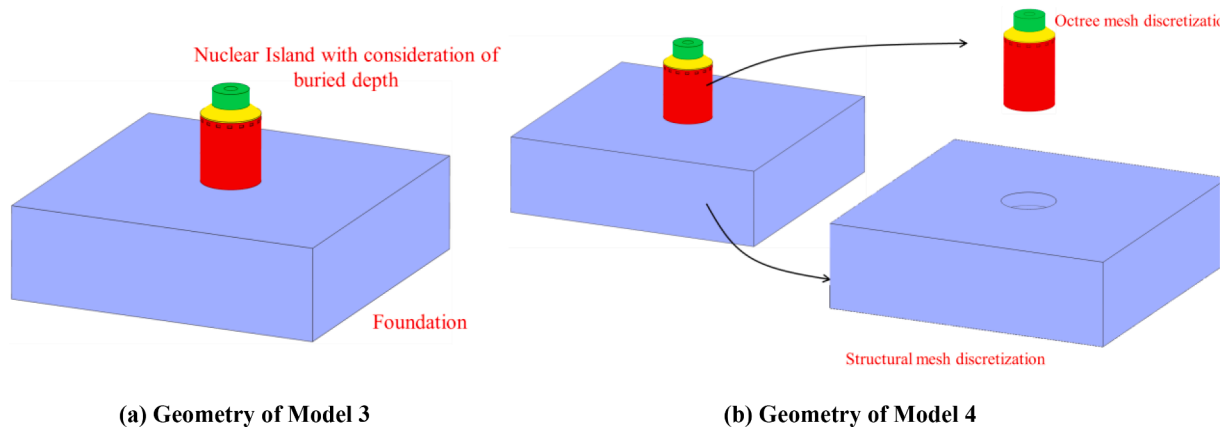


Fig. 15. Vertical verification group.

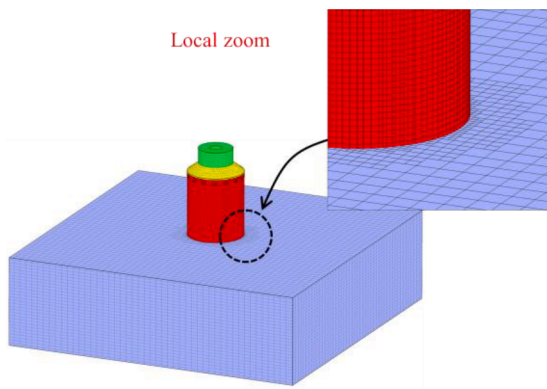


Fig. 16. Model 3: Octree mesh discretization.

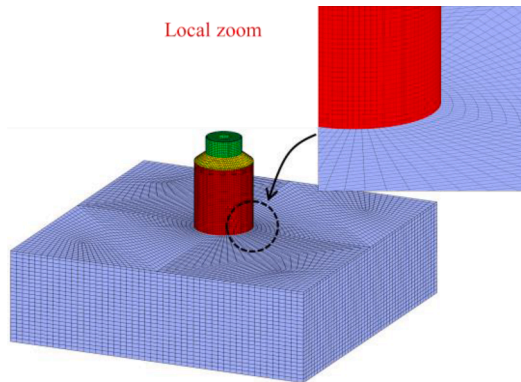


Fig. 17. Model 4: Combination bonding method.

Table 1
Details of the example verification group.

	H-group		V-group	
	Model 1	Model 2	Model 3	Model 4
NI	Octree grids	Octree grids	Octree grids	Octree grids
Foundation	Structured grids	Structured grids	Structured grids	Structured grids
Purpose	Verify accuracy in the horizontal direction		Verify accuracy in the vertical direction	

key equations necessary for explaining the solution procedure and implementation are provided here. Additionally, since the SBFEM

solution is analytical in the radial direction, it is more precise than isoparametric FEM [20]. Firstly, the elastic-static governing equations are obtained from the necessary solution procedure as shown in Fig. 2.

With the introduction of radial coordinates ξ , the boundary can be scaled radially from the scaling center (Fig. 3 and Fig. 4). For 3D problems, the displacements at a point (ξ, η, ζ) inside a pyramid can be interpolated from the displacement function $u(\xi)$, as shown in Fig. 5.

The variational principle is introduced to derive the SBFEM equation in the nodal displacement function $u(\xi)$. Simultaneously solving the equations in Fig. 2, the equilibrium equation can be expressed as:

$$E_0 \xi^2 u(\xi)_{,\xi\xi} + (2E_0 + E_1^T - E_1) \xi u(\xi)_{,\xi} + (E_1^T - E_2) u(\xi) + F(\xi) = 0 \quad (1)$$

The coefficient matrices $E_i (i = 0, 1, 2)$ depend on only the geometry and the material properties of the domain, which are evaluated for the boundary surface elements and assembled over the discretized polyhedron boundary. $F(\xi)$ is a load vector that includes only the contributions from the body loads. With the help of the Galerkin weighted residual method, the equation becomes as shown in Fig. 6. The analytical nodal displacement function $u(\xi)$ can be derived in the radial direction. To solve the SBFEM equation, a variable $X(\xi)$ that incorporates the nodal displacement function $u(\xi)$ and the nodal force function $q(\xi)$ is introduced as follows:

$$X(\xi) = \begin{Bmatrix} \xi^{0.5} u(\xi) \\ \xi^{-0.5} q(\xi) \end{Bmatrix} \quad (2)$$

Using eigenvalue decomposition, the Hamiltonian matrix Z formulated using the coefficient matrices $E_i (i = 0, 1, 2)$ and the identity matrix I can be decoupled into pairs of eigenvalues as shown in Eq. (3). The parameters ψ_u and ψ_q are the modal displacements and forces, respectively. The detailed process from Eq. (3) to Eq. (5) is in the reference [21].

$$Z = \begin{bmatrix} E_0^{-1} E_1^T - 0.5I & -E_0^{-1} \\ -E_2 + E_1 E_0^{-1} E_1^T & -(E_1 E_0^{-1} - 0.5I) \end{bmatrix} \quad (3)$$

$$Z[\psi_u \quad \psi_q]^T = [\psi_u \quad \psi_q]^T S_n \quad (4)$$

$$\Phi(\xi, \eta, \zeta) = N^u(\eta, \zeta) \psi_u \xi^{-(0.5+S_n)} \psi_u^{-1} \quad (5)$$

2.3. Octree mesh methodology

The Octree mesh methodology is a hierarchical, tree-like data structure that is used to describe a 3D space. This technique can be considered as a 3D extension of the quad-tree methodology. Further details can be found in references [22]. So far, several researchers have combined the SBFEM-based polyhedron element and the Octree technique to overcome the shape limitations of conventional elements [21,23–26].

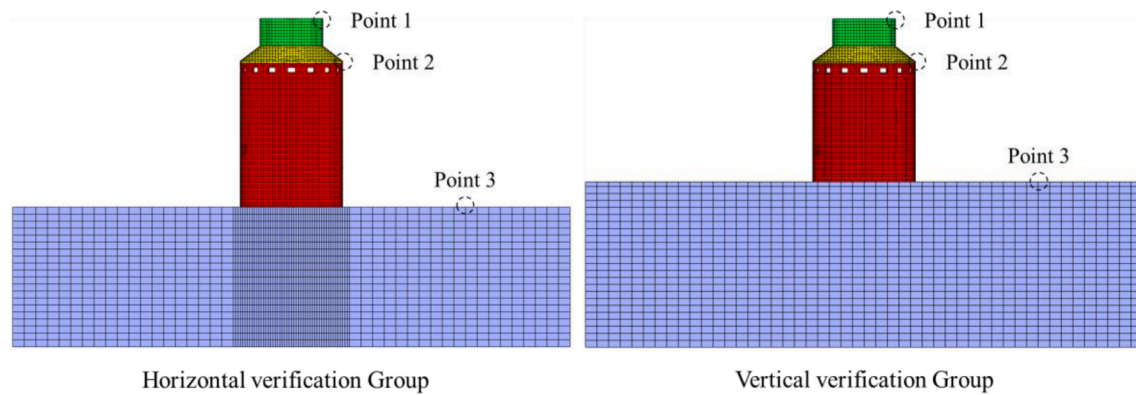


Fig. 18. Observation points of the example verification group.

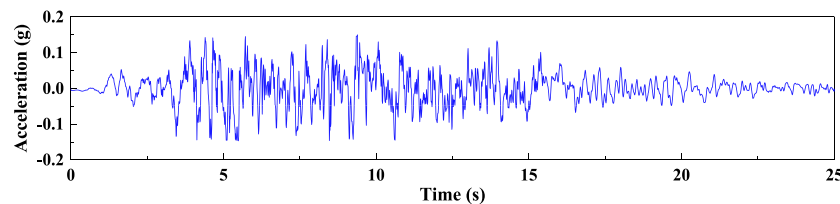


Fig. 19. Time history curve of earthquake acceleration.

Conventional isoperimetric elements such as tetrahedra, pyramids, prisms and hexahedra a fixed geometry (as shown in Fig. 7). Polyhedron elements can possess an arbitrary shape (as shown in Fig. 8), thus bypassing the limitation of the conventional discrete elements (e.g. hexahedrons, pentahedrons and tetrahedrons). By leveraging the advantages of the polyhedron, cross-scale transitions in the finite element model can be efficiently and smoothly implemented. Furthermore, the discretization process is amenable to a high degree of automation.

3. Combination method of structured and octree grids

3.1. Octree discrete model

In our prior work [18], the whole shield building is modelled with Octree grid discretization. The segmented volume models divided according to different materials and assembly components were meshed automatically. However, the prior approach had some deficiencies. As shown in Fig. 9(a) for circular structures, polygons divided the circle in the process of octree discretization, which precludes meshing in the radial direction. As shown in Fig. 9(b), other research efforts found that during the discretization of slender members a fine symmetry mesh size could not be satisfied.

3.2. Combination bonding method

Traditional structured grids include geometries such as tetrahedra, hexahedra, etc. Structured grids are suitable for circular, slender, and thin-walled structures and components, all of which require regular and fine grids. On the other hand, the Octree discrete method has a strong advantage in solving complex bodies. In order to leverage the advantages of both methods, this paper intends to develop a discrete method to combine structured grid and octree grid to establish more precise and efficient models.

In the combined method, circular and slender members are discretized using structured grids while other structures are discretized using Octree grids. The two different types of grids are then adhered together at the interfaces (Fig. 10). The method only remeshes the grids of the contact surface without changing the existing grids in the rest of

the structures. After adding new nodes and edges on the contact surface, SBFEM is used to construct complex polyhedron elements.

Fig. 11 demonstrates an example of the combination process in which regions 1 and 2 are targeted for combination. First, the contact surface is determined through contact bonding relationship, then error tolerance is set and unmatched nodes and edges are inserted. Relatively small elements and short edges can be deleted to improve the computational reliability. Finally, the scaled boundary finite polyhedron elements are used to construct the contact surface polyhedron elements after the reconstruction.

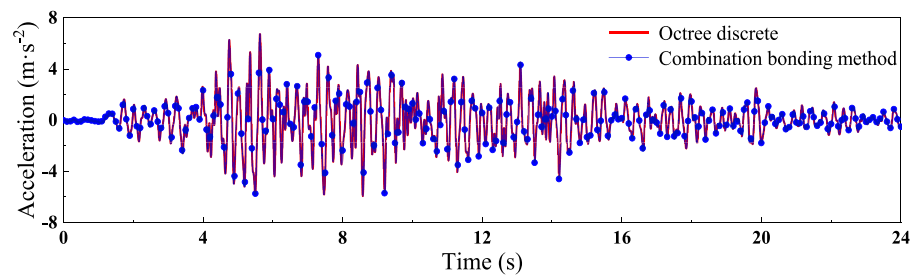
This method benefits from the advantages of both structure grid and octree grid discrete methods. With efficient independent modelling and free flexible combination, the method can provide cross-scale interfacing of different grid sizes. In particular it does not require modifications to existing meshes when new structures are components are added to the model. Thus, the method can effectively facilitate the rapid establishment of refined, whole system models of nuclear power plants.

3.3. Numerical example

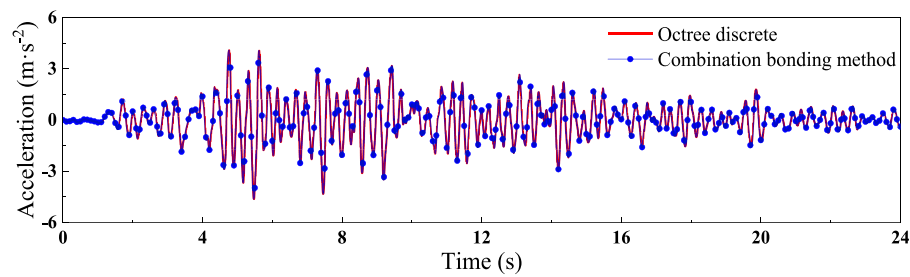
The method above need to verify computationally. Two groups, including horizontal combination bonding group and vertical combination bonding group are set up. These groups are respectively referred to as “H-group” and “V-group” in the following. The purpose of the “H-group” is to verify that the proposed combined bonding method generates accurate data in the horizontal direction. While the “V-group” is for the vertical direction.

The “H-group” Model 1 (Fig. 12(a)), which is composed of an overall model of the Nuclear Island (NI) and the foundation, which is meshed with an octree discrete grid. Fig. 13 shows the mesh obtained after the octree discretization of Model 1. In “H-group” Model 2 (Fig. 12(b)), the NI is discretized using octree gridding while the foundation is discretized using structured grid. The two parts in Model 2 are then combined. Fig. 14 shows the mesh after the combination bonding of Model 2.

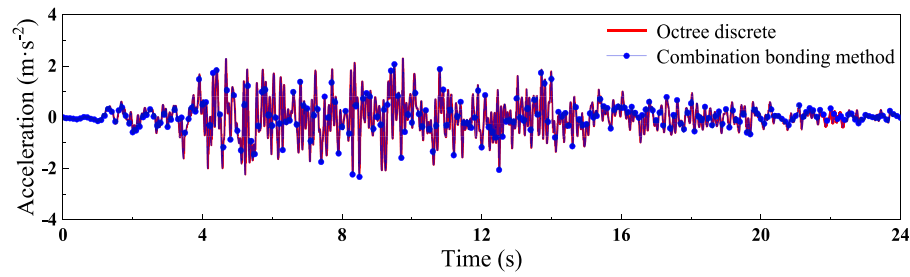
The “V-group” Model 3 (Fig. 15 (a)). The model considers the buried depth of the NI, and the model is meshed via octree discretization. Fig. 16 shows the grid obtained the Octree discretization of Model 3. In “V-group” Model 4 (Fig. 15 (b)), the NI is meshed through Octree



(a) Observation point 1

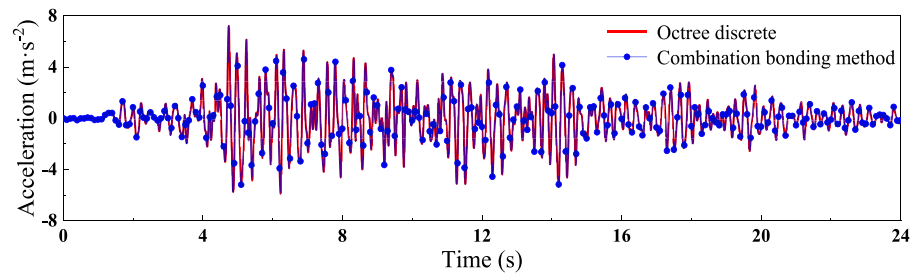


(b) Observation point 2

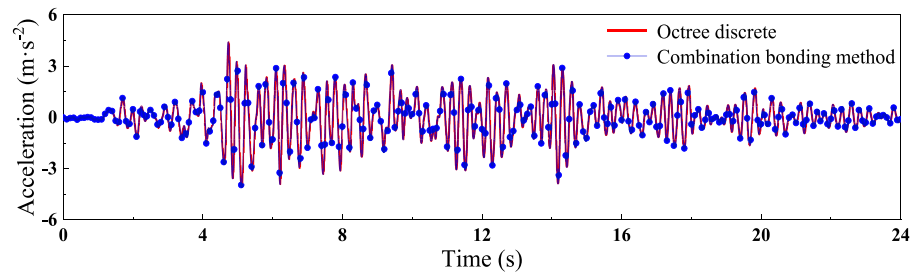


(c) Observation point 3

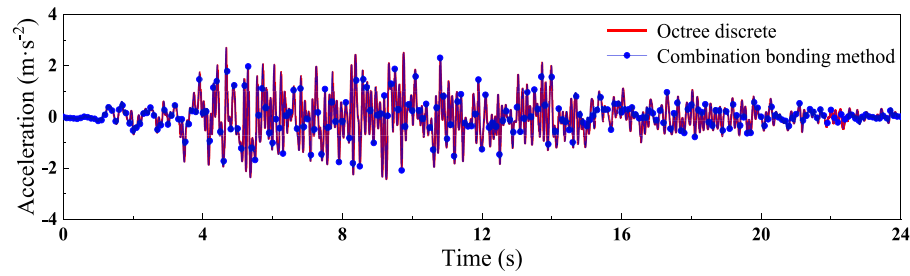
Fig. 20. The acceleration time history curves in H-group.



(a) Observation point 1



(b) Observation point 2



(c) Observation point 3

Fig. 21. The acceleration time history curves in V-group.

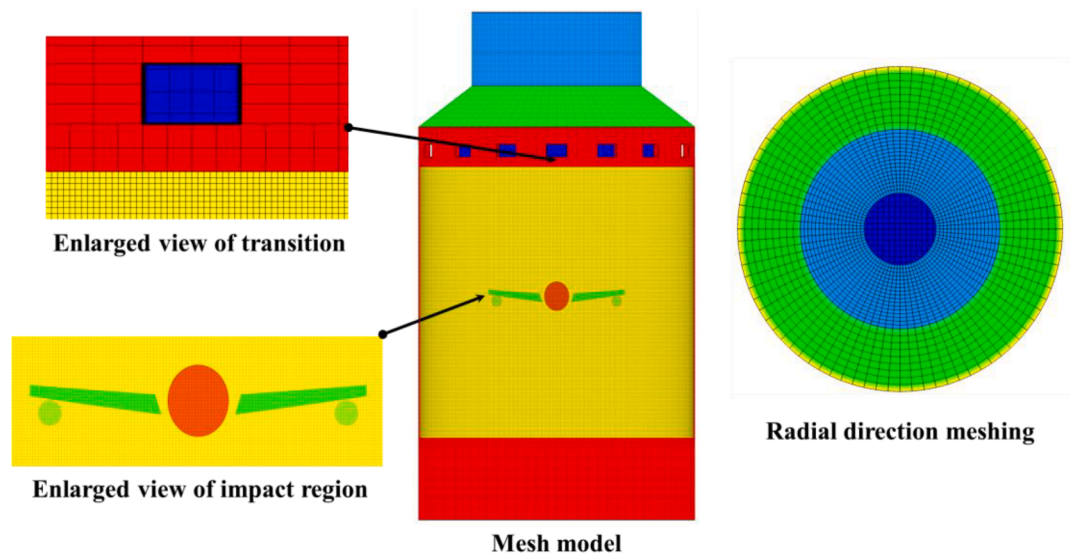


Fig. 22. Structured grids of the shield building.

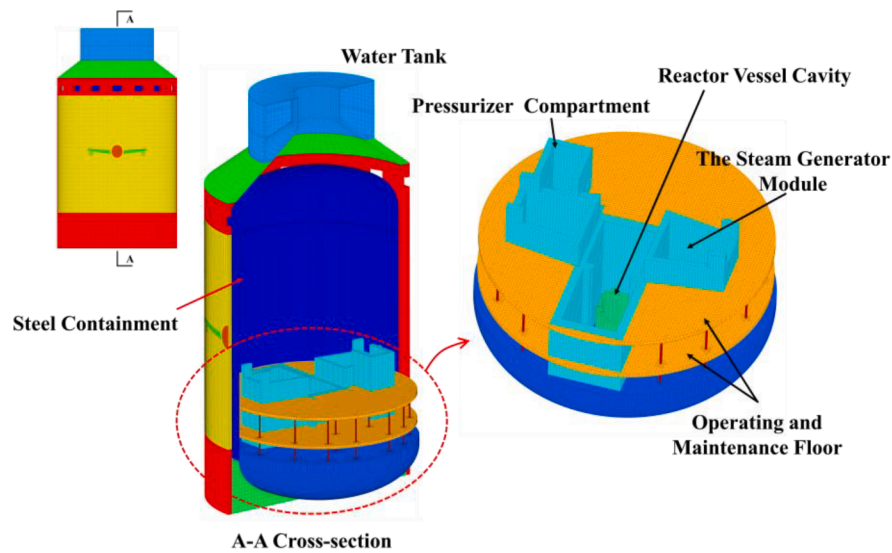


Fig. 23. Internal structure of reactor building.

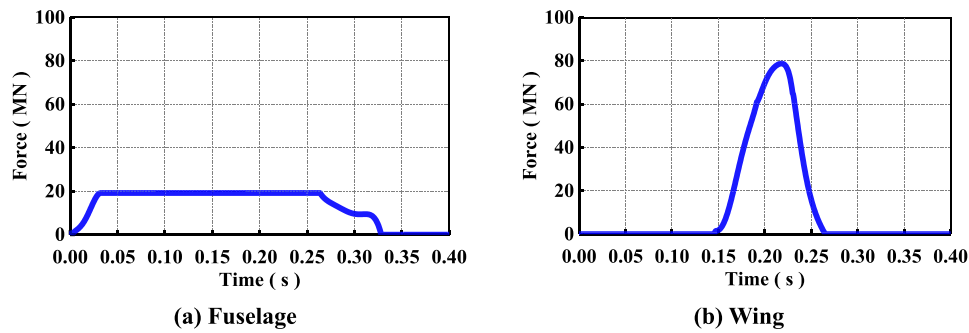


Fig. 24. Aircraft impact force time-history curve.

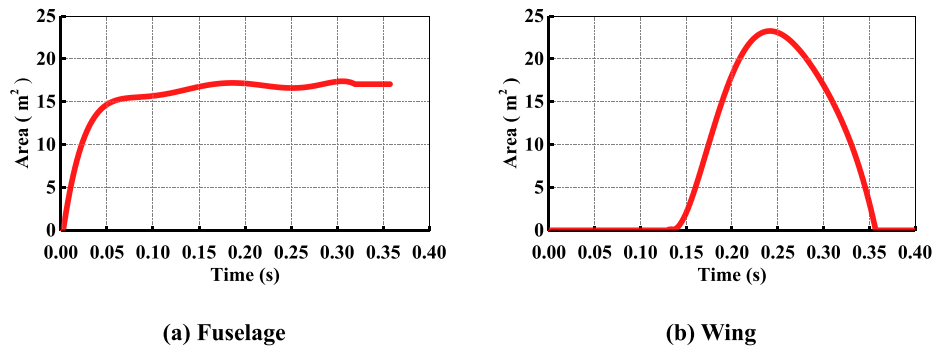


Fig. 25. Aircraft impact area time-history curve.

Table 2
Concrete Parameters.

Material	Parameter	Value
Concrete	Mass density	2400 kg/m ³
	Shear modulus	32.5 GPa
	Poisson's ratio	0.2
	Compressive strength	27.6 MPa
	Tensile pressure	3.26 MPa
Steel CV	Mass density	7800 kg/m ³
	Young's modulus	2.06×10^5 MPa
	Poisson's ratio	0.3

discretization while the foundation is meshed with structured grids. The components are then combined. Fig. 17 shows the grid after the combination bonding of Model 4.

Table 1 summarizes the characteristics of the verification groups. Fig. 18 shows the locations of observation points in the two verification groups. The concrete in the NI has an elastic modulus of 3.25×10^4 MPa, Poisson's ratio of 0.2, and density of 2400 kg/m³. The foundation is a lithologic foundation with a density of 2450 kg/m³, elastic modulus of 1.5×10^4 MPa and Poisson's ratio of 0.28. The seismic wave originated from the RG1.60 spectrum over a duration of 25 s is shown in Fig. 19. The seismic input method used is the uniform excitation method (combined seismic inertia force and constrained boundary). In addition,

considering that it is used for validation, unidirectional ground motion is adopted.

The software used for verification calculation above and dynamic analysis in following sections in this research is GEOGYNA[27,28], which is a high-performance computational system developed by the Institute of Earthquake Engineering at the Dalian University of Technology. Fig. 20 compares results from each observation point of Model 1 (octree method) and Model 2 (combination method) in the “H-group”. It can be seen that time history curves almost completely coincide, thus verifying the accuracy of the method in the horizontal direction. Likewise, Fig. 21 overlays observations from Model 3 (octree method) and Model 4 (combination method) in the “V-group”. The coinciding of the curves also verifies the accuracy of the combination method in the vertical direction.

In summary, with the advantage to combine and bond different element types, the method proposed successfully achieves node addition and element reconstruction.

4. Response of internal structure during impact

4.1. Model utilizing the combined bonding method

After verifying the accuracy of the proposed combined bonding method, the computational model to be used in this study is established.

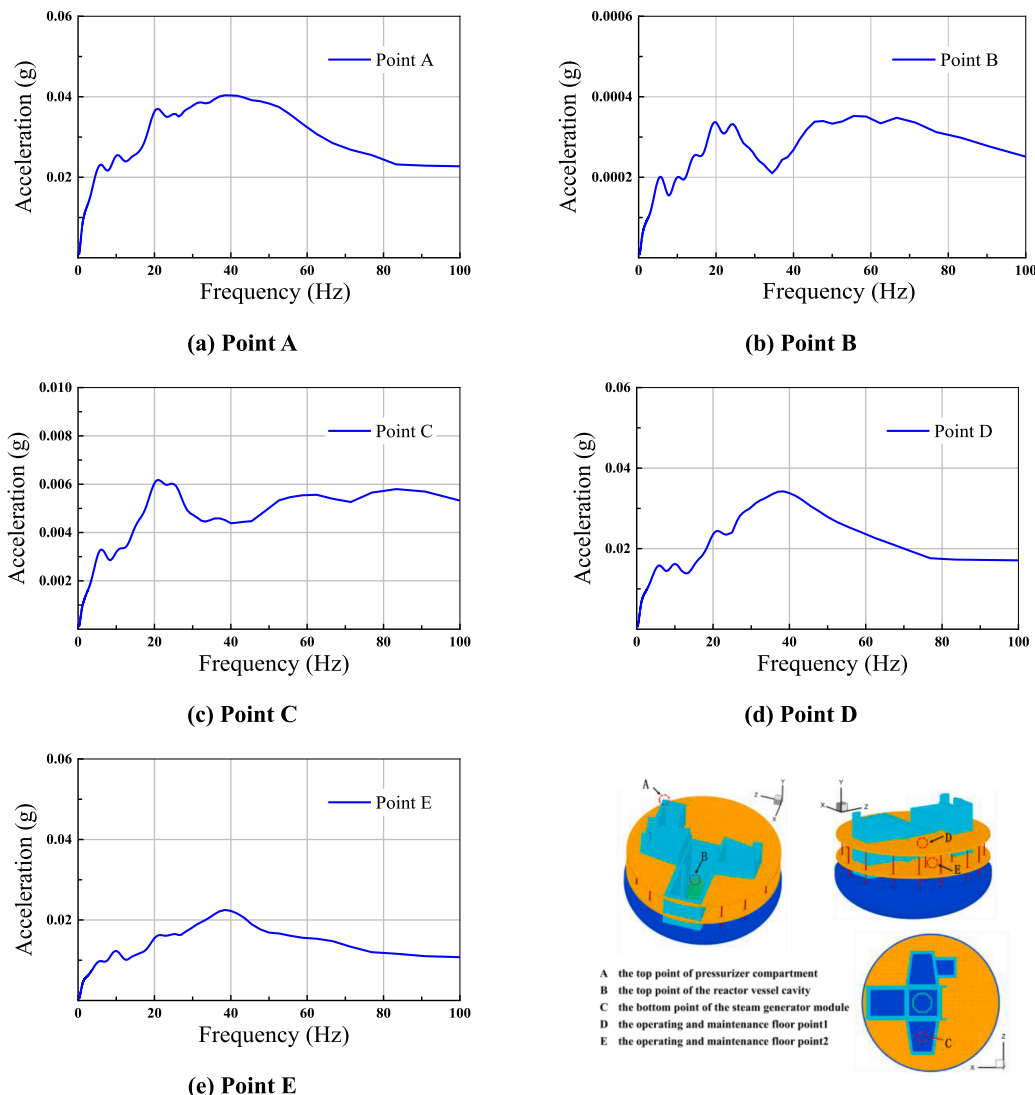


Fig. 26. The acceleration response spectrum result of observation points.

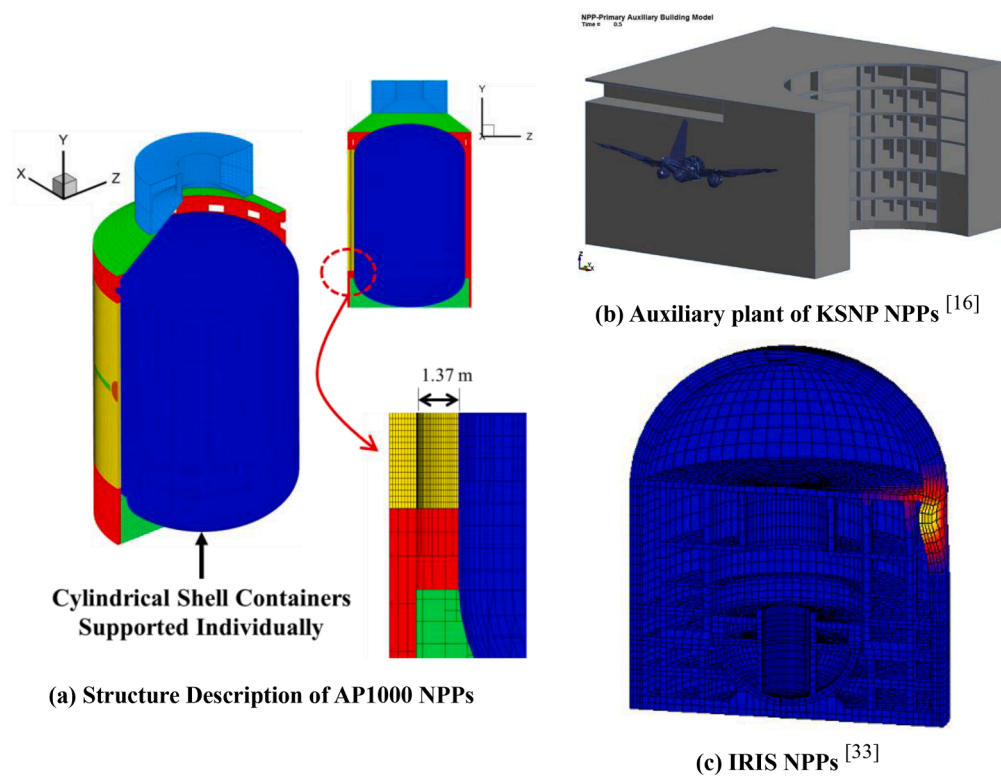


Fig. 27. Other models from literature. (a) Structure Description of AP1000 NPPs. (b) Auxiliary plant of KSNP NPPs [16]. (c) IRIS NPPs [33]

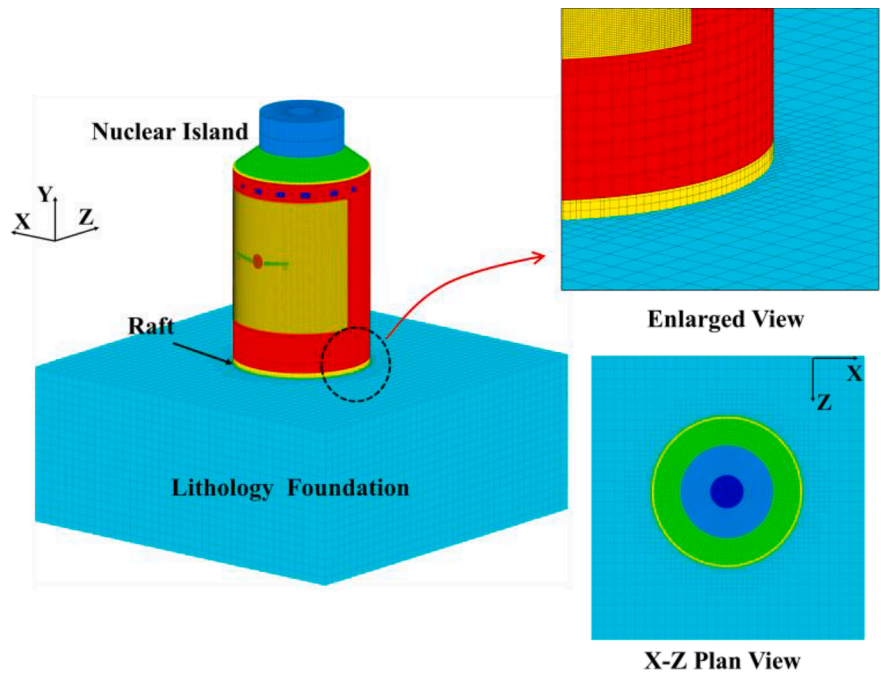


Fig. 28. Model with lithologic foundation.

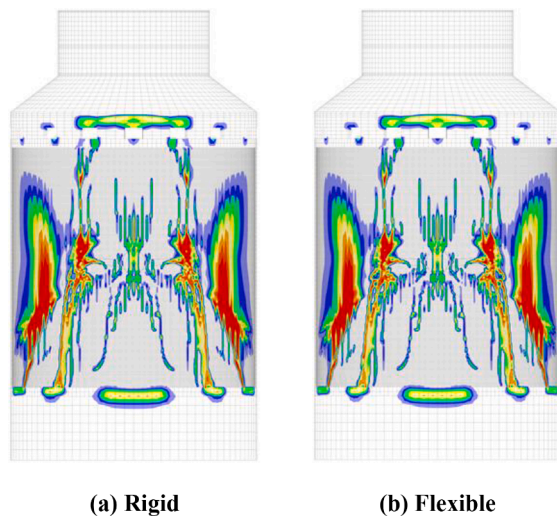


Fig. 29. The damage situation of shield building in external perspective.

During the aircraft impact on nuclear power plants, it is necessary to analyze the damage of the shield building and the effect of vibration on the internal structures. The external shield building is a cylindrical structure. In order to perform radial meshing, structured grid discretization is adopted (Fig. 22). The mesh of the impact zone and the transition zone requires a fine size, and thus combination bonding method can be conveniently used to integrate meshes of different sizes (see enlarged view of Fig. 22). Meanwhile, the reactor building in the model includes the pressurizer compartment, steam generators module (CA01), the reactor vessel cavity (CA04), the operating and maintenance floor and other important internal structures. Due to the complexity in the spatial characteristics of the internal structure, the octree grid discretization method is adopted.

Fig. 23 shows the final step, the components are combined using the proposed combination method. The model has 916,747 cells and 1,104,036 nodes.

4.2. Aircraft force and material parameters

The load curve derived from relevant research [29] and HAD101/04 [30] issued by the National Nuclear Safety Authority of China, which details codes pertaining to nuclear power plant safety. According to the characteristics of commercial aircraft, the impact effects can be divided

into two parts, the fuselage and the wing. The fuselage collided with the structure, followed by the wings about 0.13 s later. Based on the code's appendix, the force time-history curve and impact area time-history curve for a Boeing 707-320 aircraft are shown in Fig. 24 and Fig. 25. Although these aircraft types are obsolete, they are still official and are thus imported in this study.

An increase in strength due to high strain rates from the impact-induced, rapid deformation should be considered for the analysis of the concrete containment vessel. In general, the static strength values should be increased by using Dynamic Increase Factors (DIFs). According to the NEI07-13 reports [17], the compressive strength DIF is 1.15 and the tensile strength DIF is 1.20. Concrete failure is assessed using the plastic damage model, which can describe the complex behaviour of concrete (27.6 MPa and 3.26 MPa compressive and tensile strengths, respectively) subjected to large strains and high pressures [31]. In addition, the analysis utilizes the smeared model that is often adapted to simulate complex reinforced concrete structures. In the smeared model, the reinforcement is smeared uniformly in each concrete element, and the smeared element can be considered as continuous and homogeneous material [32]. Table 2 lists the material parameters and values of the smeared concrete element.

4.3. Dynamic response of the internal structures

Five observation points, including node A at the top of pressurizer compartment, node B at the top of the reactor vessel cavity, node C at the bottom of the steam generator module, and node D and E at the operating and maintenance floor, are selected to observe the vibration responses of the internal structure during the impact. Each observation points of the floor response spectrum (impact direction are only organized) over the 0.4 s impact duration after applying force–time history analysis (FTHA) are shown in Fig. 26.

The figure shows that the acceleration responses of all nodes are weak, especially at observation point C (peaked at 0.006 g). However, despite the nodes at the bottom of the shield building are fully constrained at the rigid boundary conditions, results from the models reported other researchers [16] show quite intense. To appreciate how these difference arose, Fig. 27 summarizes the models in other major research, where Fig. 27(a) is the shield building model of AP1000, Fig. 27(b) is the auxiliary plant of the KSNP Nuclear Power Plant in South Korea, and Fig. 27(c) shows the IRIS (International Reactor Innovative and Secure) advanced light water pressurized water reactor building.

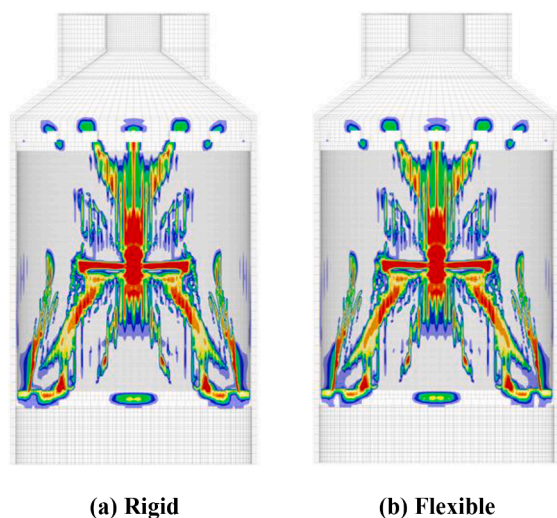


Fig. 30. The damage situation of shield building in internal perspective.

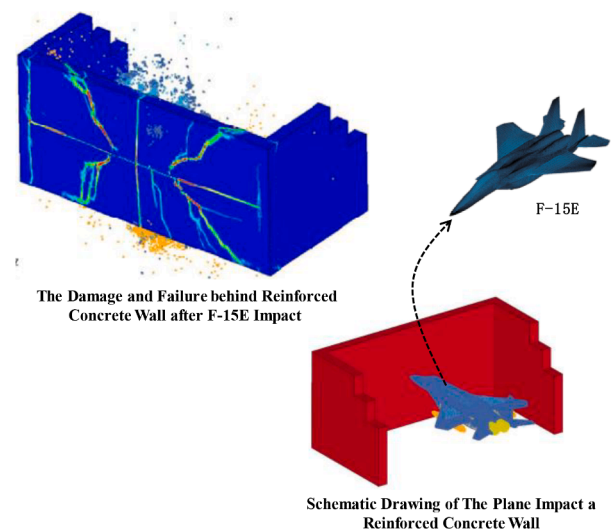
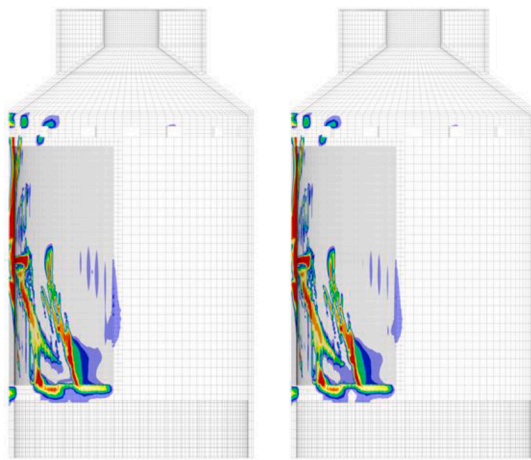


Fig. 31. The damage of a reinforced concrete wall subjected by an F-15E fighter jet [34].



(a) Rigid

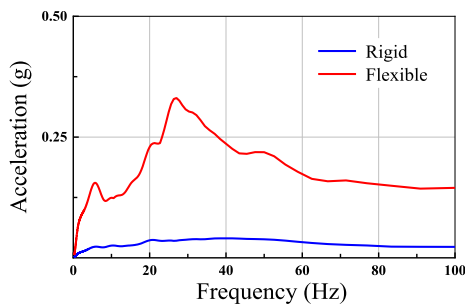
(b) Flexible

Fig. 32. The damage of shield building in center section.

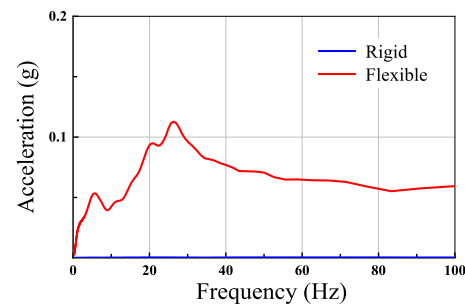
As seen in the figures, the impact for the KSNP power plant occurs on the wall of the auxiliary building, which is connected to the floor slab. Likewise, for the IRIS power plant, the containment vessel is directly connected to the internal structures. Due to such structural form, the impact force from the aircraft is transmitted directly to the floor slab. However, the internal structure of the AP1000 reactor building is located in a separate cylindrical steel shell vessel. Meanwhile, the steel containment vessel is not directly connected to the external shield building (i.e. 1.37 m distance). Instead, the vessel is connected to the external building only by the foundation structure, and thus if rigid boundaries are used, the amount of vibration transmitted from the external shield to the internal structures via the foundation are greatly diminished.

4.4. Model with foundation

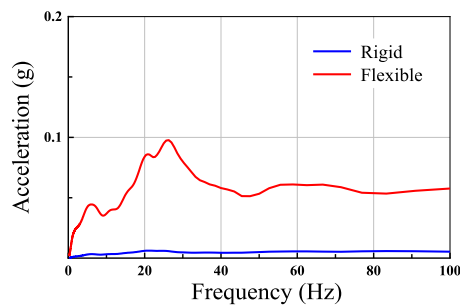
The concrete base mat and the foundation at the bottom of the NI are built together as shown in Fig. 28. The foundation is lithologic with a bedrock density of 2450 kg/m^3 , elastic modulus of $1.5 \times 10^4 \text{ MPa}$ and Poisson's ratio of 0.28. The size of the foundation is $140 \text{ m} \times 140 \text{ m}$ in the horizontal plane and 60 m in the vertical direction. There are 959,528 cells and 1,152,076 nodes in the model.



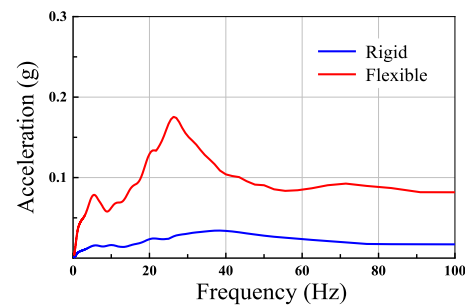
(a) Point A



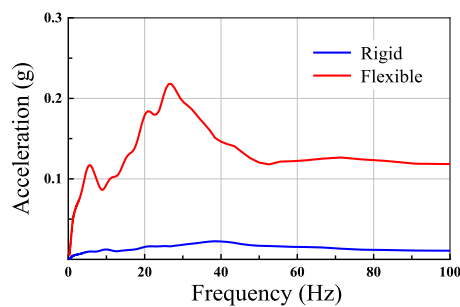
(b) Point B



(c) Point C



(d) Point D



(e) Point E

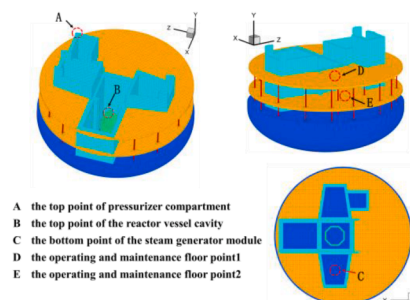


Fig. 33. The acceleration response spectra result of observation points in the model with foundation.

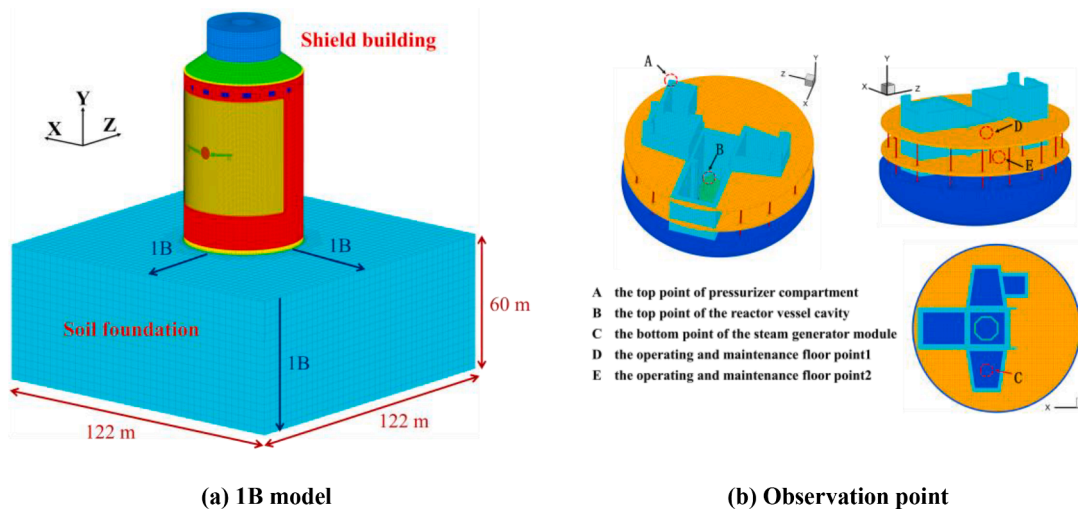


Fig. 34. The 1B model and the locations of the observation points.

4.5. Influence of SSI effect on structural responses of reactor building

In order to properly analyze the effects of impact-induced vibration on the internal structure, it is necessary to first understand the details of the damage situation of the shield building and determine whether the presence of bedrock affects the damage characteristics and expansion of the shield building. Fig. 29 shows the front view of the damage experienced by the shield building when the foundation is either rigid or flexible. It is noted that the legend presents the degree of damage used by tensile damage factor, which is taken from the concrete plastic damage model. The figure shows that the damage in the wing and engine position is the most significant and extends downwards. The damage region extends diagonally upward and downward, and are nearly identical for both foundation types. Fig. 30 shows the damage from internal perspective. An asterisk-shaped damage area can be seen behind the impact area, and the damage extends downward towards of the engine region. A report about the impact of F-15 jet fighters [34] (Fig. 31), which is one of the few studies that look at the internal perspective of the damage, also presented an asterisk-shaped damage area on the internal face of the wall. The damage region and the extent of the impact-induced damage area on the internal face are similar for both foundation types.

Finally, the sectional view of the damage is presented in Fig. 32. The damage distribution of the wall along the radial direction and the elevation direction of the shield building are almost the same. Based on the above analysis, it can be concluded that the assumption of a flexible

foundation does not affect the damage situation. Moreover, the key issue for deformation analysis have studied carefully in our previous research [18].

Fig. 33 shows the floor response spectra at each observation point when the foundation is flexible versus when the foundation is rigid. The responses of all observation points increase significantly when the foundation is lithologic. The maximum acceleration (0.33 g) occurs at node A, followed by node E at 0.22 g. The acceleration responses of observation points B, C and D are 0.11 g, 0.10 g and 0.18 g, respectively. The peak frequency of the acceleration response spectrum at each observation point is concentrated around 25 Hz.

5. The reasonable truncation range

5.1. Models with different foundation sizes

Soil-structure interaction has a great influence on the impact-induced vibration response of the internal structure of the reactor building. Therefore, it is necessary to analyze both the acceptable ranges of sizes for the foundation and type of artificial boundary conditions.

Using the height $B = 66$ m of the steel containment vessel as a reference, the foundation extends 1B (Fig. 34), 2B and 3B in horizontal and vertical directions respectively. Fig. 35(a) shows a 2B model, which has 1,118,936 elements and 1,328,036 nodes, and Fig. 35(b) shows a 3B model, which has 1,404,260 elements and 1,621,953 nodes. To avoid the influence of scattered waves reflecting at the boundary, a

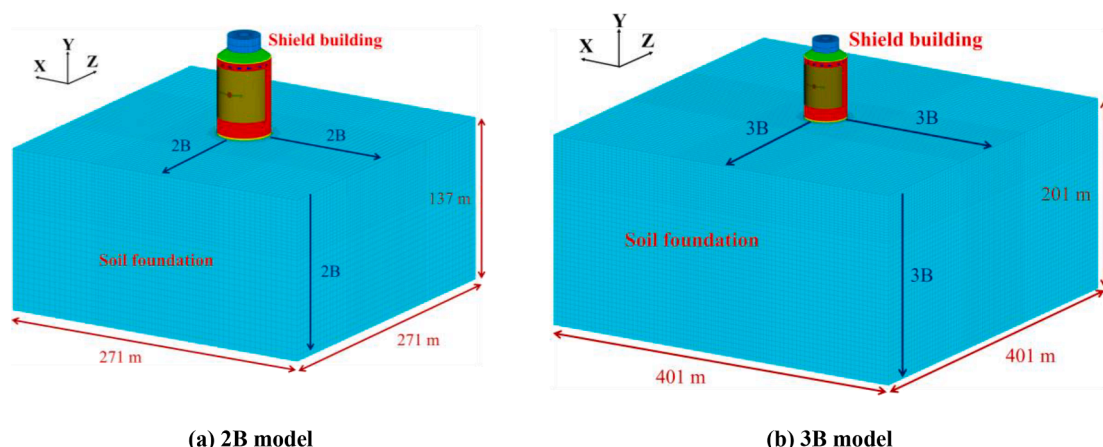


Fig. 35. Perspective views of the 2B and 3B models.

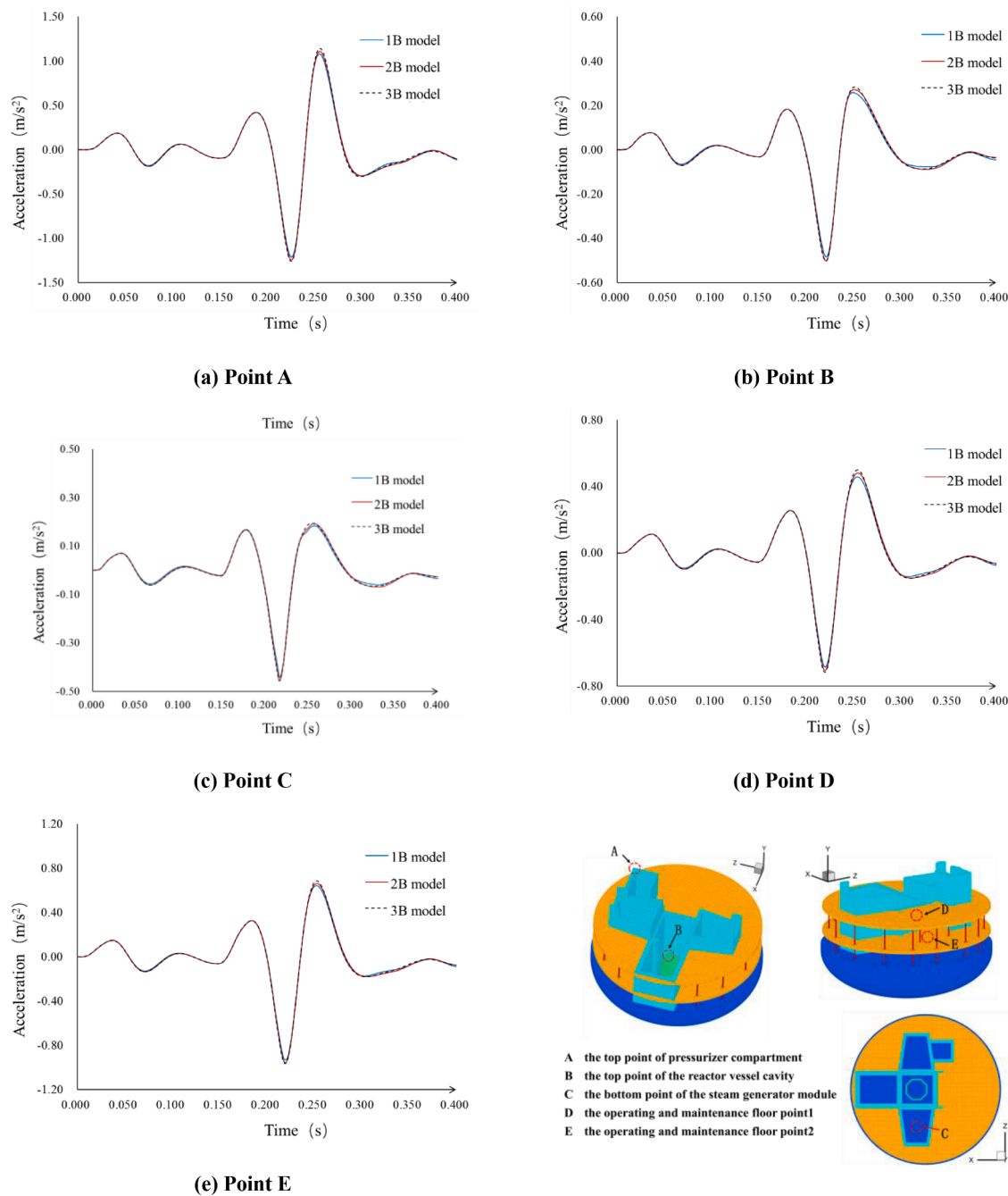


Fig. 36. The acceleration response spectrum result of observation points in the model with foundation.

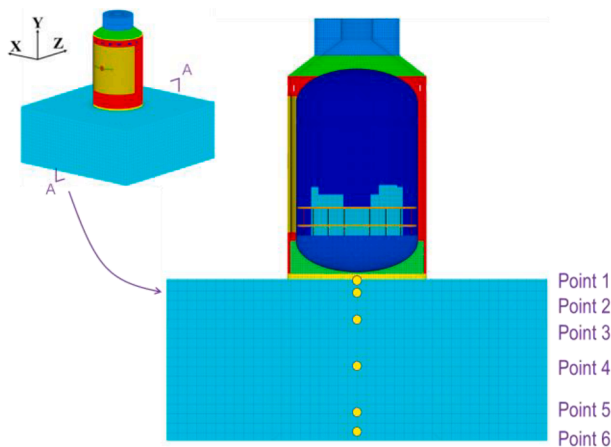


Fig. 37. The calculation model with foundation (1B model).

viscoelastic artificial boundary is applied at the edges of the foundation in all models to absorb the vibration energy transmitted by the upper structure. The parameters of artificial boundary are set according to the previous section.

5.2. Investigating the acceptable size ranges of the foundation

The time-history curves of the acceleration at the observation points for all models are plotted in Fig. 36. The plots show that the accelerations for all nodes are nearly identical across the three models, with slightly more differences in the peak accelerations.

The results demonstrate the minimal influence of the foundation size on the response spectra. Thus, further analysis and research are needed to determine the reasons for this outcome. The sectional view of the 1B computational model is shown in Fig. 37. Points 1–6 are successively set along the direction of foundation depth, and the acceleration time history results of each observation point are shown in Fig. 38. In the figure, the time of peak acceleration is delayed in correlation with the depth, thus providing some insight into the nature of vibration propagation in the foundation. In addition to delays, the vibration also weakens at deeper depths (i.e. 0.25 m/s^2 at Point 1 and 0.01 m/s^2 at Point 6) during the propagation process due to the action of foundation damping.

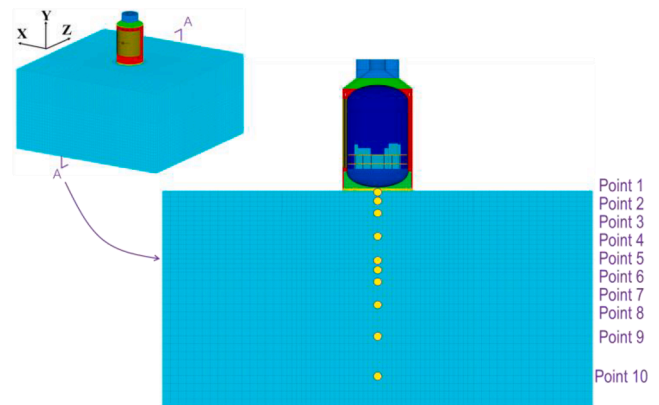


Fig. 39. The computational model with foundation (2B model).

Point 6 of the 1B model is too close to the bottom boundary, and thus to avoid the influence of the boundary on the results, the larger 2B model (Fig. 39) is used and more points are observed. Similar to the 1B model, the observation points (Points 1–10) are set along the direction of foundation depth. In addition, the acceleration time-history of all observation points are shown in Fig. 40. Similar to the 1B model, the time of peak acceleration is more delayed and the intensity of the acceleration is more attenuated if the observation point is deep (i.e. Point 10 is very weak at 0.009 m/s^2). In addition, Point 6 in the 2B model has a similar acceleration (0.02 m/s^2) as the 1B model. The above observations suggest that vibrations have trouble propagating long distances in the foundation possibly due to the damping of the foundation.

If the damping of the foundation plays a major role in the response of the model, there is a need to see whether the form of the boundary contributes a secondary influencing factor. Therefore, we return to the 1B model and perform testing with rigid boundaries versus absorbing boundaries. The resulting acceleration time-history curves are shown in Fig. 41, and it can be seen that the accelerations of all observation points are almost the same. Thus, the artificial boundary conditions have limited impact on the accelerations.

Next, an analysis of the influence of foundation damping parameters on vibration is needed. In the analysis, the damping ratio of the

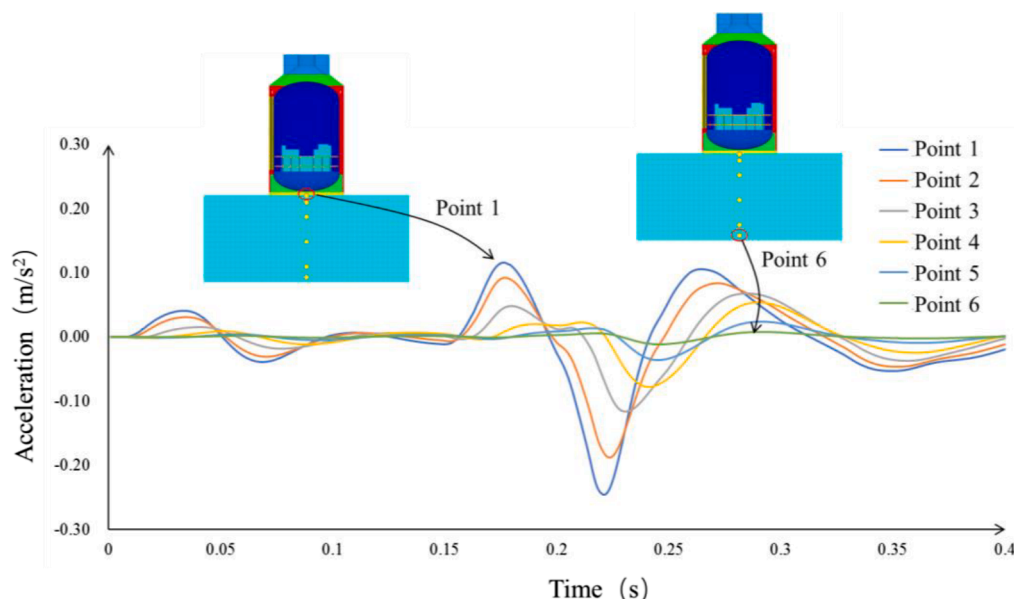


Fig. 38. The calculation model with foundation.

foundation is adjusted from 5 % to 0.1 % to observe whether vibration propagation is affected by the reduction of damping. The 1B model is still used, and a viscoelastic artificial boundary is set at the edges of the foundation. The computed results are shown in Fig. 42. The results show that the acceleration of each observation point experienced significant changes due to changes in the damping ratio. This observation aligns with the previous theory that the damping of the foundation improved the vibration response of the mode. The results so far demonstrate that the foundation size in the 1B model is adequate for studying the vibration response of the NI due to aircraft impact.

5.3. Evaluation of dynamic responses

In order to further evaluate the influence of the vibration on the internal structures, it is necessary to define certain criteria. As there is no agreed upon reference standard for safety requirements and what conditions should trigger a shutdown, this paper preliminarily uses a procedure based on the EPRI NP-5930 [35] report. This report provides the following two-level criterion for determining whether the Operating Basis Earthquake (OBE) has been exceeded:

- 1) Response spectrum check: the ground response spectrum (5 % damping ratio) for the motion at the site exceeds the corresponding OBE design response spectrum or 0.20 g, whichever is greater;
- 2) Cumulative absolute velocity (CAV) check: the computed CAV value from the ground motion is greater than 0.3 g*s. CAV is defined as follows:

$$CAV = \int_0^{t_{\max}} |a(t)| \cdot dt \quad (3.1)$$

where $a(t)$ is the acceleration response time history, t_{\max} is the duration.

Although this procedure has been originally used for the seismic safety assessment of a NPP, it can also be used to assess the safety conditions of the NPP subjected to the aircraft crash.

Fig. 43(a) and (b) respectively show the response spectrum of each observation node in cases of rigid foundation and flexible foundation. The accelerations of the rigid foundation model are generally weak, so the comparison with OBE are not discussed. For the model with flexible foundation, if 0.20 g is used as the evaluation standard (dotted line in the figure), then node A (at the top of pressurizer compartment) and node E (at the operating and maintenance floor) have exceeded the critical value. Furthermore, the CAV values of each node are plotted in

Fig. 44, which shows that the maximum CAV value is only 0.011 g *s. According to the reference standard, although the peak value of the response spectrum exceeds the safety standard, the CAV is less than the threshold value of 0.30 g *s and thus no alarm is needed.

However, it should be noted from the CAV equation that the integral is dependent on time. Since earthquakes have significantly longer duration than an aircraft impact, the integral value for the aircraft impact will be significantly smaller. Therefore, further research and more detailed evaluation criteria are needed to determine whether the evaluation criteria obtained solely from seismic studies is reasonable.

6. Conclusion

This paper established an advanced computational model of an advanced Generation III + nuclear island through the use of a novel combined bonding technique. The new model is used to investigate the dynamic response of the internal structures in the nuclear island when an aircraft has impacted the shield building. The following conclusions can be drawn from the results:

- 1) The remeshing algorithm developed for contact surfaces only requires a secondary mesh discretization performed on the contact surface. The proposed method method utilizes the superiority of SBFEM polyhedral elements to fully leverage the advantages of Octree and structured grid discretization methods. Through the method, individual components can be meshed independently and freely interfaced with each other, thus allowing cross-scale combination of different mesh sizes.
- 2) Since the shield building is connected to the internal structures only by the foundation structure, results obtained from the rigid foundation are distorted. The results became more realistic when SSI effects (i.e. the addition of a flexible foundation) were taken into account. Therefore, SSI effects must be considered when analyzing the vibration response of AP1000 NPPs.
- 3) A foundation size of $B \times B \times B$, where B is the height of the steel containment vessel, satisfies accuracy requirements. Furthermore, the results indicate that the damping ratio of the foundation plays a key role in vibration propagation.

Funding

National Natural Science Foundation of China (No.51279025,

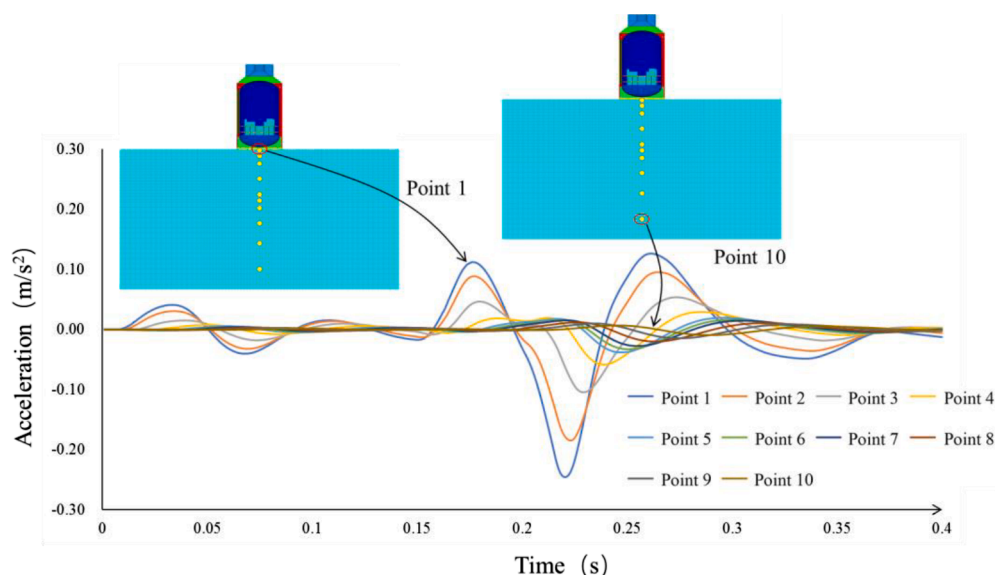


Fig. 40. The calculation model with foundation.

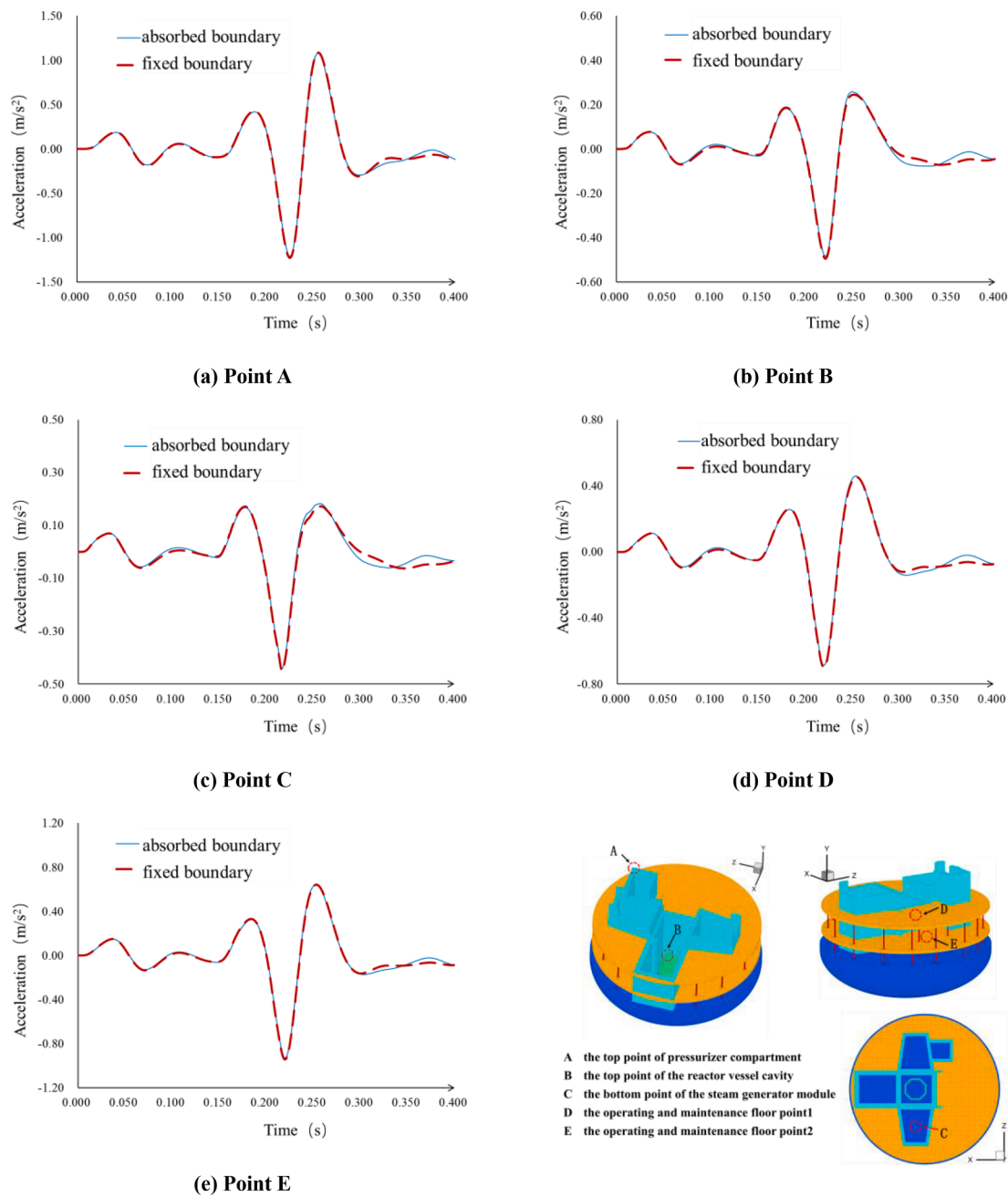
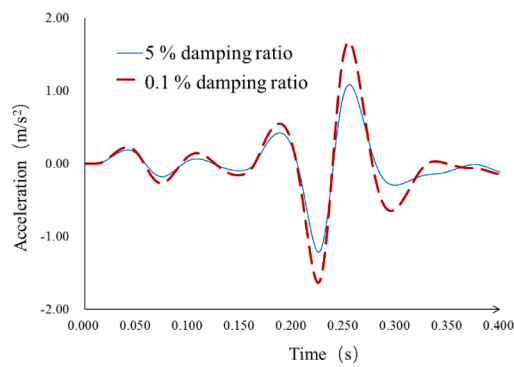
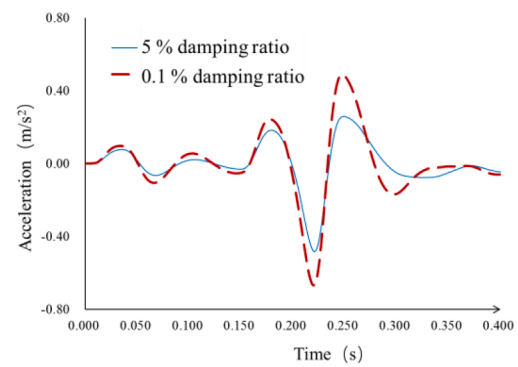


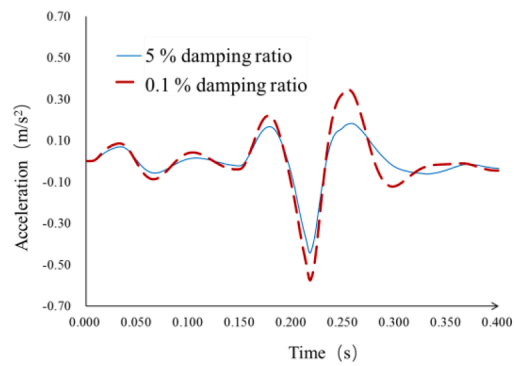
Fig. 41. The acceleration response spectrum result of observation points in the model with foundation.



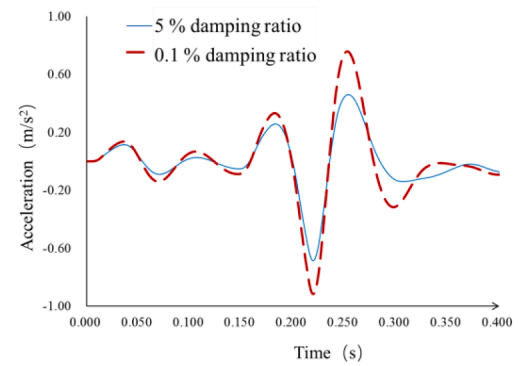
(a) Point A



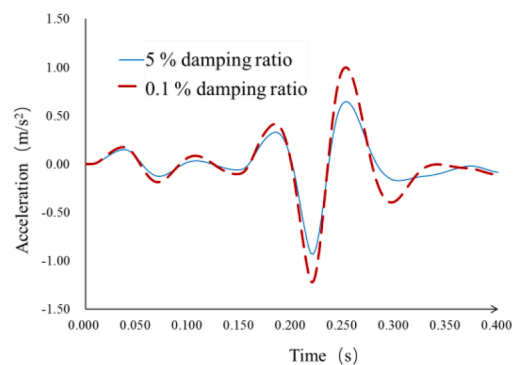
(b) Point B



(c) Point C



(d) Point D



(e) Point E

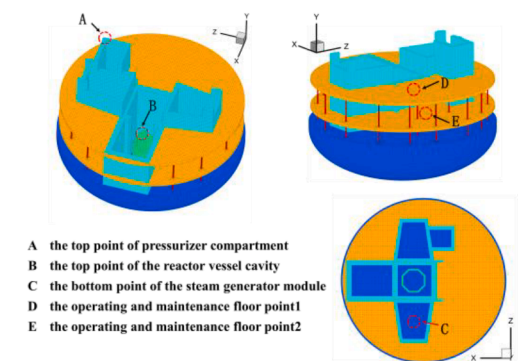


Fig. 42. The acceleration response spectrum result of observation points in the model with foundation.

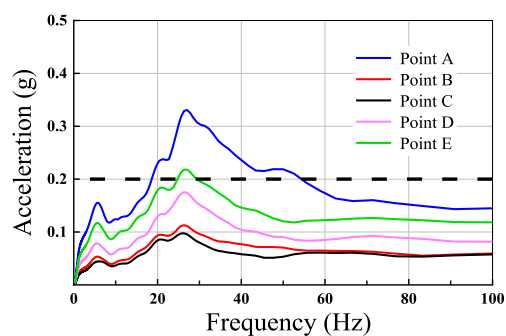


Fig. 43. The observation points response results.

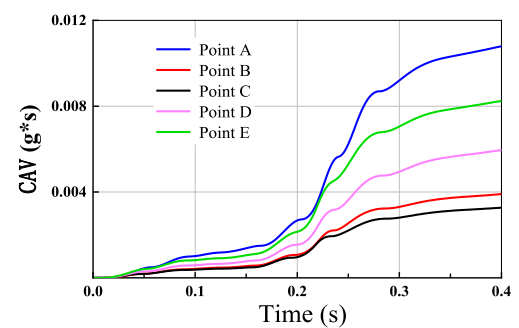


Fig. 44. Absolute cumulative velocity response results (flexible foundation).

91215301); Program for New Century Excellent Talents in University (NCET-12-0083).

Declaration of Competing Interest

The authors declare that they have no known competing financial interests or personal relationships that could have appeared to influence the work reported in this paper.

Acknowledgements

This work was supported by the Fundamental Research Funds for the Central Universities (Grant No. DUT21RC(3)099). This financial support is gratefully acknowledged.

References

- [1] International Atomic Energy Agency. Nuclear Power Reactors in the World[R]., 2019.
- [2] United States Nuclear Regulatory C. Aircraft impact assessment: 10CFR50.150[S]. Washington, D.C., 2009.
- [3] Nnsa. Safety Regulations for Nuclear Power Plant Design. The National Nuclear Safety Administration of China: HAF 102-2016[S]. Beijing, 2016.
- [4] Lee K, Jung J, Hong J. Advanced aircraft analysis of an F-4 Phantom on a reinforced concrete building[J]. Nucl Eng Des 2014;273:505–28.
- [5] Arros J, Doubalski N. Analysis of aircraft impact to concrete structures[J]. Nucl Eng Des 2007;237(12):1241–9.
- [6] Jin B M, Lee Y S, Jeon S J, et al. Development of finite element model of large civil aircraft engine and application to the localized damage evaluation of concrete wall crashed by large civil aircraft[C]. The 21st International Conference on Structural Mechanics in Reactor Technology. Delhi, India: 2011.
- [7] Zhang T, Wu H, Fang Q, et al. Influences of nuclear containment radius on the aircraft impact force based on the Riera function[J]. Nucl Eng Des 2015;293: 196–204.
- [8] Siefert A, Henkel FO. Nonlinear analysis of commercial aircraft impact on a reactor building—Comparison between integral and decoupled crash simulation[J]. Nucl Eng Des 2014;269:130–5.
- [9] Lin F, Tang H. Nuclear containment structure subjected to commercial aircraft crash and subsequent vibrations and fire[J]. Nucl Eng Des 2017;322:68–80.
- [10] International Atomic Energy Agency (IAEA). Safety aspects of nuclear power plants in human induced external events: general considerations[R]. Safety Reports Series No.86, Vienna, Austria, 2017.
- [11] International Atomic Energy Agency (IAEA). Safety aspects of nuclear power plants in human induced external events: margin assessment[R]. Safety Reports Series No.88, Vienna, Austria, 2017.
- [12] Petrangeli G. Large airplane crash on a nuclear plant: Design study against excessive shaking of components[J]. Nucl Eng Des 2010;240(12):4037–42.
- [13] Kostov M, Henkel FO, Andonov A. Safety assessment of A92 reactor building for large commercial aircraft crash[J]. Nucl Eng Des 2014;269:262–7.
- [14] Henkel FO, Klein D. Variants of Analysis of the Load Case Airplane Crash[C]. International Association for Structural Mechanics in Reactor Technology, SMIRT19. Toronto, Canada: IASMiRT; 2007.
- [15] Shin SS, Hahm D, Park T. Shock vibration and damage responses of primary auxiliary buildings from aircraft impact[J]. Nucl Eng Des 2016;310:57–68.
- [16] Thai D, Kim S. Safety assessment of a nuclear power plant building subjected to an aircraft crash[J]. Nucl Eng Des 2015;293:38–52.
- [17] Nuclear Energy I. Methodology for performing aircraft impact assessments for new plant designs: NEI07-13[S]. Washington DC, 2009.
- [18] Zou D, Sui Y, Chen K, et al. A cross-scale refined damage evolution analysis of large commercial aircraft crashing into a nuclear power plant[J]. Struct Design Tall Spec Build 2019;28(16):e1668.
- [19] Chen K, Zou D, Kong X, et al. Elasto-plastic fine-scale damage failure analysis of metro structures based on coupled SBFEM-FEM[J]. Comput Geotech 2019;108: 280–94.
- [20] Song C. The Scaled Boundary Finite Element Method: Introduction to Theory and Implementation[M]. John Wiley & Sons Ltd., 2018.
- [21] Chen K, Zou D, Kong X. A nonlinear approach for the three-dimensional polyhedron scaled boundary finite element method and its verification using Koyna gravity dam[J]. Soil Dyn Earthq Eng 2017;96:1–12.
- [22] Saputra AA, Birk C, Song C. Computation of three-dimensional fracture parameters at interface cracks and notches by the scaled boundary finite element method[J]. Eng Fract Mech 2015;148:213–42.
- [23] Zou D, Teng X, Chen K, et al. A polyhedral scaled boundary finite element method for three-dimensional dynamic analysis of saturated porous media[J]. Eng Anal Bound Elem 2019;101:343–59.
- [24] Zou D, Chen K, Kong X, et al. An approach integrating BIM, octree and FEM-SBFEM for highly efficient modeling and seismic damage analysis of building structures [J]. Eng Anal Bound Elem 2019;104:332–46.
- [25] Chen K, Zou D, Kong X, et al. An efficient nonlinear octree SBFEM and its application to complicated geotechnical structures[J]. Comput Geosci 2018;96: 226–45.
- [26] Chen K, Zou D, Kong X, et al. Global concurrent cross-scale nonlinear analysis approach of complex CFRD systems considering dynamic impervious panel-rockfill material-foundation interactions [J]. Soil Dyn Earthq Eng 2018;114:51–68.
- [27] Xu B, Zou D, Kong X, et al. Dynamic damage evaluation on the slabs of the concrete faced rockfill dam with the plastic-damage model[J]. Comput Geotech 2015;65: 258–65.
- [28] Zou D, Sui Y, Chen K. Plastic damage analysis of pile foundation of nuclear power plants under beyond-design basis earthquake excitation[J]. Soil Dyn Earthq Eng 2020;136:106179.
- [29] Iqbal MA, Sadique MR, Bhargava P, et al. Damage assessment of nuclear containment against aircraft crash[J]. Nucl Eng Des 2014;278:586–600.
- [30] External Man-Induced Events for Nuclear Power Plant Sitting[S]. Beijing, 1989.
- [31] Yu X, Kong X, Zou D, et al. Linear elastic and plastic-damage analyses of a concrete cut-off wall constructed in deep overburden[J]. Comput Geotech 2015;69:462–73.
- [32] Zhao C, Chen J, Xu Q. Dynamic analysis of AP1000 shield building for various elevations and shapes of air intakes considering FSI effects subjected to seismic loading[J]. Prog Nucl Energy 2014;74:44–52.
- [33] R. Lo Frano G F.. Preliminary evaluation of aircraft impact on a near term nuclear power plant[J]. Nucl Eng Des 2011;241(12):5245–50.
- [34] Wilt T, Chowdhury A. Response of reinforced concrete structures to aircraft crash impact[R]. San Antonio, Texas: Southwest Research Institute; 2011.
- [35] Benjamin J. R., And Associates. EPRI. NP-5930: a criterion for determining exceedance of the operation basis earthquake[R]. Palo Alto, California: Electric Power Research Institute; 1988.